

# Engineering Eigenstates in High-Overtone Bulk Acoustic Resonators

Master's Thesis

Pedro Rosso Gómez

## Supervisors

Prof. Dr. Yiwen Chu

Dr. Hugo Michiel Doeleman

Dr. Rodrigo da Silva Benevides

Hybrid Quantum Systems Group  
Laboratory for Solid State Physics  
D-PHYS, ETH Zürich  
August 26, 2022

## Acknowledgements

First and foremost, I would like to thank Yiwen for giving me the opportunity to work in her research group and making this whole project possible, and for always being available for insightful discussions which helped me complete this important step in my life.

I would also like to thank Thomas, my predecessor, who recruited me for this project; Max and Uwe for teaching me the insider tips of cleanroom work; Stefano for embarking on the journey to restructure the BeamProp codebase and for the wonderful discussions over the snacks breaks; Ines, Matteo, Marius, Yu, Tom, Arianne, Giacomo, Francesco, Leo, Emre, Dmitry, Michael, Mona, Johannes, and Alessandro for the wonderful time spent inside and outside the office.

I would also like to thank the FIRST Team, especially PD Dr. Silke Schön and Petra Burkard for their help over the whole project, the Euler Cluster Support Team for their guidance for setting up the simulations on the cluster, and the laser writer expert, Ekaterina Al-Tavil for her patience.

Last but definitely not least, I would like to thank Hugo and Rodrigo for the dedication, patience and support over the last months. I cannot put into words the appreciation I have for all the feedback, discussions, and the amount of time invested into my project.

I would like to dedicate this work to my parents, Max and Vivien, to my sister Olivia, and to all my grandparents, Enrico, Juan, Luiza and Sonia.

# Contents

<b>1</b>	<b>Introduction</b>	<b>5</b>
1.1	The need for quantum information processing . . . . .	5
1.2	Quantum acoustics for quantum information processing . . . . .	5
1.3	Specific applications of this project . . . . .	6
<b>2</b>	<b>Solid mechanics fundamentals</b>	<b>7</b>
2.1	Strain and stress tensors . . . . .	7
2.2	Stress-strain relation . . . . .	9
2.3	Christoffel's equation and the slowness surface . . . . .	10
<b>3</b>	<b>High-overtone bulk acoustic resonators (HBARs)</b>	<b>13</b>
3.1	Paraxial wave approximations . . . . .	13
3.2	The effective horizontal velocity . . . . .	15
3.3	Stability criteria . . . . .	17
<b>4</b>	<b>Numerical simulations</b>	<b>19</b>
4.1	Frequency domain simulations (BeamProp) . . . . .	19
4.1.1	Adding a secondary material layer . . . . .	22
4.1.2	Limitations . . . . .	23
4.1.3	Implementation and performance analysis . . . . .	24
4.2	Optical Schrödinger Equation (OSE) simulations . . . . .	26
4.2.1	Implementation and performance analysis . . . . .	30
4.3	Simulation results . . . . .	31
4.3.1	Optical Schrödinger Equation . . . . .	31
4.3.2	BeamProp . . . . .	33
4.4	Anharmonic dome shapes . . . . .	36
4.4.1	Perturbation theory . . . . .	36
4.4.2	OSE Simulations . . . . .	39
<b>5</b>	<b>Fabrication tools</b>	<b>41</b>
5.1	Grayscale Lithography . . . . .	41
5.1.1	Masked grayscale lithography . . . . .	42
5.1.2	Direct-written laser grayscale lithography . . . . .	44
5.1.3	From graytones to height profiles . . . . .	44
5.1.4	From height profiles to graytones . . . . .	47
5.2	Solvent reflow . . . . .	48

<b>6 Sample measurements</b>	<b>49</b>
6.1 Masked grayscale lithography . . . . .	49
6.1.1 Calibration arrays . . . . .	49
6.1.2 Domes . . . . .	49
6.1.3 Calibration correction . . . . .	52
6.1.4 Reflow optimization . . . . .	55
6.2 Direct written laser lithography . . . . .	55
<b>7 Conclusion</b>	<b>57</b>
7.1 Outlook . . . . .	58

# Chapter 1

## Introduction

### 1.1 The need for quantum information processing

In the age of information, the pursuit of more processing power is one of the main drivers of innovation and spending; although the latter has reached astronomical levels in the latest years, we are still limited by our computers when it comes to certain mathematical problems. The current strategy of increasing the number of transistors in a computer chip will probably have to be replaced in the near future by other approaches, as these logical units have already been reduced to few nanometers in size [1]; further reductions result in unwanted quantum-mechanical effects such as electrons tunneling into and out of the transistors [2].

While some avoid dealing with the complications arisen from quantum mechanics, others attempt to tame this beast. The main reason? A machine that can fully leverage quantum-mechanical properties such as entanglement and superposition is nothing short of groundbreaking. On the theoretical side, quantum algorithms can outperform its classical counterparts [3, 4], quantum annealing can solve non-convex optimization problems more efficiently [5], and the simulation of quantum systems in actual quantum systems promises more accurate predictions [6], with applications ranging from enhanced pharmaceutical drug development to the discovery of novel phases in matter [7].

On the experimental side, the quest for control of quantum-mechanical systems is already past its initial steps, with notable progress in different approaches [8], such as superconducting qubits [9, 10, 11], color centers [12], trapped ions [13] and photons [14, 15, 16]. A quantum machine that can effectively solve problems faster than the current supercomputing clusters requires long qubit coherence times, low error rates, high gate fidelities and quantum links capable of transmitting quantum information between computing nodes. The previously mentioned architectures fulfill each requirement to a certain extent; none fulfills all of them completely.

### 1.2 Quantum acoustics for quantum information processing

Mechanical systems, in particular high-overtone bulk acoustic resonators (HBARs), are promising candidates for solving some of the aforementioned challenges. Their high quality factors (Q-factors) enable the physical realization of long-lived phononic modes, whose lifetimes can exceed superconducting qubits' [17, 18]. In addition, mechanical resonators can interact with electromagnetic systems through various types of interactions,

which include but are not limited to piezoelectricity, capacitive coupling, and Brillouin scattering [19]. These two characteristics have spanned two new fields of research centered around hybrid optomechanical systems:

1. Circuit quantum acousto-dynamics (cQAD), which is based on the bilinear interaction between non-linear superconducting qubits and mechanical resonators. Applications range from quantum mechanical control of mechanical modes of motion [20] to the long storage of quantum information, for example, in a quantum random access memory (qRAM).
2. Quantum optomechanical transduction [21, 22], which consists in creating a link between superconducting circuits, a highly developed platform for quantum computing, to a very convenient carrier of quantum information, optical photons, using mechanical resonators as an intermediate.

In summary, the different physical couplings in mechanical systems allows the connection of different quantum systems for the fabrication of hybrid devices, which can leverage the advantages of each subsystem simultaneously.

### 1.3 Specific applications of this project

Any connection between mechanical resonators and other systems such as superconducting qubits or photons requires a physical interaction. From our quantum mechanics classes, we remind ourselves that the coupling between quantum states is governed by two aspects:

1. Spatial overlap between the states
2. Temporal overlap during the interaction period<sup>1</sup>

HBARs have several acoustic modes; any of them can couple to the systems of interest. Unwanted couplings reduce the qubit's lifetime, which is exactly what the envisioned quantum machine from the previous section should avoid. Achieving this goal requires a deep knowledge of the HBAR's spectrum, both in frequency and in real space. We wish to increase the coupling strength to an arbitrary mechanical mode and at the same time avoid any coupling to other unwanted modes.

The main objectives of this project is to combine simulation techniques and novel fabrication methods to fabricate HBARs with interesting eigenmode spectra matching the predicted values from simulation and to use said tools to generate HBARs that maximize the coupling to a mechanical mode of interest while avoiding coupling to any other modes, hence increasing the coherence times and fidelity of the mechanical quantum states.

---

<sup>1</sup>This criterion is inherently more flexible, e.g. for a tunable qubit and a mechanical mode of a resonator with respective frequencies  $\omega_q$  and  $\omega_m$ , one can couple both resonantly ( $\omega_q = \omega_m$ ) or off-resonantly / dispersively ( $\omega_q = \omega_m + \Delta$ ).

# Chapter 2

## Solid mechanics fundamentals

Before we start talking about high overtone bulk acoustic resonators (HBARs), we need to understand the peculiarities of sound beam propagation in crystals. This intermezzo in solid mechanics introduces the necessary concepts up to the slowness surface; it's shape describes the propagation of harmonic waves in crystal, and it will be the starting point for many derivations. This section will mostly follow [23].

### 2.1 Strain and stress tensors

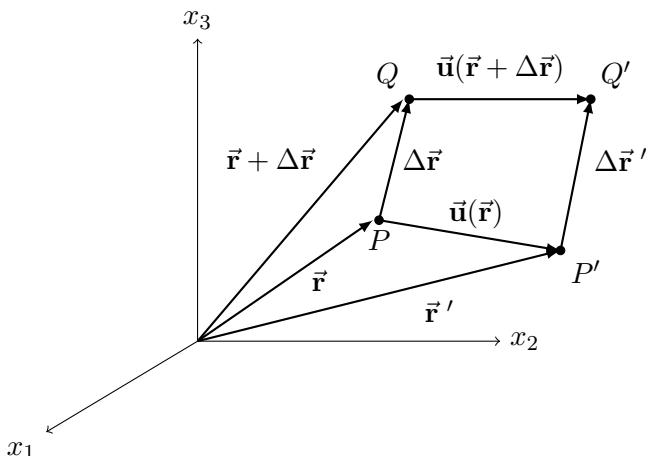


Figure 2.1: Schematic definition of the relative displacement  $\vec{u}(\vec{r})$ , adapted from [23].

Solid mechanics is the science of deformable objects: we consider solids that can change their shape under external forces, while still retaining their overall structure. Furthermore, we only consider forces below the solids' elastic limit: in the absence of said forces, the object returns to its original shape. When an object is strained (see figure 2.1), a point \$P\$, fixed in the object, will shift to a different point \$P'\$. This shift can occur due to the rigid translation and rotation of the object, but here we are interested in shifts due to strain in the object. The strain-induced displacement of \$P'\$ with respect to \$P\$ is displacement vector

$$\vec{u} = \vec{r}' - \vec{r} \quad (2.1)$$

which varies with position  $\vec{r}$  within the body, and is time-dependent, so we write it as

$\vec{u}(\vec{r}, t)$ . The center of mass, which is the origin of our coordinate system, is assumed to have zero strain-induced displacement, so that  $\vec{u}(0, t) = 0$ .

Suppose now we have two points,  $P$  and  $Q$  (as shown in figure 2.1), separated by  $\Delta\vec{r}$ ; under strain  $P$  displaces to  $P'$  and  $Q$  displaces to  $Q'$ . We want an expression for the spatial variation  $\Delta\vec{u}$  for infinitesimally small displacements  $\Delta\vec{r}$ . We can perform a Taylor expansion

$$u_i(\vec{r} + \Delta\vec{r}) = u_i(\vec{r}) + \sum_{j=1}^3 \frac{\partial u_i}{\partial x_j} \Delta r_j + \mathcal{O}(\Delta r_j^2) \quad (2.2)$$

The partial derivatives are functions of space and time. We can collect them all in a special tensor, namely the displacement tensor  $D$

$$D = \nabla \vec{u} = \begin{bmatrix} \frac{\partial u_1}{\partial x_1} & \frac{\partial u_1}{\partial x_2} & \frac{\partial u_1}{\partial x_3} \\ \frac{\partial u_2}{\partial x_1} & \frac{\partial u_2}{\partial x_2} & \frac{\partial u_2}{\partial x_3} \\ \frac{\partial u_3}{\partial x_1} & \frac{\partial u_3}{\partial x_2} & \frac{\partial u_3}{\partial x_3} \end{bmatrix} \quad (2.3)$$

We break it up into two pieces, the symmetric and the antisymmetric part

$$D = S + \Omega \quad (2.4)$$

$$S = \frac{1}{2} \left( \nabla \vec{u} + (\nabla \vec{u})^T \right) \quad (2.5)$$

$$\Omega = \frac{1}{2} \left( \nabla \vec{u} - (\nabla \vec{u})^T \right). \quad (2.6)$$

The symmetric part is the strain tensor  $S$ , and the anti-symmetric part is the rotation tensor  $\Omega$ . We can summarize the results in index notation:

- Displacement Tensor

$$D_{ij} = \frac{\partial u_i}{\partial x_j} \quad (2.7)$$

- Strain Tensor

$$S_{ij} = \frac{1}{2} \left( \frac{\partial u_i}{\partial x_j} + \frac{\partial u_j}{\partial x_i} \right) \quad (2.8)$$

- Rotation Tensor

$$\Omega_{ij} = \frac{1}{2} \left( \frac{\partial u_i}{\partial x_j} - \frac{\partial u_j}{\partial x_i} \right) \quad (2.9)$$

The description of forces acting on a solid, deformable object requires the additional knowledge of the location and spatial orientation of said forces on the surfaces and within the volume of the object. We define the stress as the force applied per unit area, and introduce the stress tensor  $T_{ij}$  as shown in figure 2.2. Diagonal elements represent compression and tension, and non-diagonal elements represent shear. Using the second Newtonian law, some symmetries and iterating over several components, one can show that the stress tensor is symmetric

$$T_{ij} = T_{ji} \quad (2.10)$$

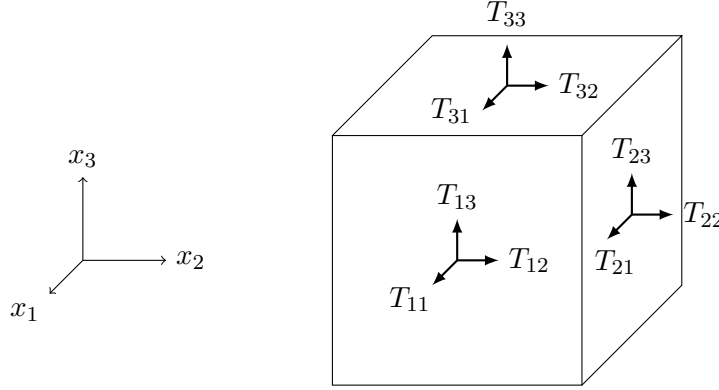


Figure 2.2: Schematic definition of the Stress tensor, adapted from [23].

## 2.2 Stress-strain relation

For most crystals at equilibrium, the atoms will position themselves at the minimum of the potential generated by the other atoms. This external potential will be quadratic in the lowest order of the displacement  $u(\vec{r})$ , and hence any corresponding force will be linear in displacement. Taking into account the whole crystal, we arrive at the linear stress strain relation

$$T_{ij} = \sum_{k=1}^3 \sum_{l=1}^3 c_{ijkl} S_{kl} \quad (2.11)$$

It holds for most materials under small displacements. At large strain, however, all materials become non-linear. At first the stiffness tensor  $c_{ijkl}$  seems to have 81 independent components, but we remind ourselves that  $S_{ij}$  and  $T_{ij}$  are both symmetric, reducing the number of independent values to 36. Furthermore, for crystals with certain symmetries, this number is even smaller. We will introduce the Voigt notation: Given that we are working with symmetric  $3 \times 3$  tensors, we will convert them into 6-dimensional vectors:

$$\begin{bmatrix} T_{11} & T_{12} & T_{13} \\ T_{21} & T_{22} & T_{23} \\ T_{31} & T_{32} & T_{33} \end{bmatrix} = \begin{bmatrix} T_1 & T_6 & T_5 \\ T_6 & T_2 & T_4 \\ T_5 & T_4 & T_3 \end{bmatrix} \quad (2.12)$$

$$\implies T = (T_1, T_2, T_3, T_4, T_5, T_6) \quad (2.13)$$

Similarly:

$$S = (S_1, S_2, S_3, \textcolor{orange}{2}S_4, \textcolor{orange}{2}S_5, \textcolor{orange}{2}S_6) \quad (2.14)$$

We will use both conventional ( $T_{ij}$ ) and Voigt notations ( $T_i$ ) from now on. Using the latter, we can finally write equation 2.11 as

$$T_\alpha = \sum_{\beta=1}^6 c_{\alpha\beta} S_\beta \quad c = \begin{bmatrix} c_{11} & c_{12} & c_{13} & c_{14} & c_{15} & c_{16} \\ c_{21} & c_{22} & c_{23} & c_{24} & c_{25} & c_{26} \\ c_{31} & c_{32} & c_{33} & c_{34} & c_{35} & c_{36} \\ c_{41} & c_{42} & c_{43} & c_{44} & c_{45} & c_{46} \\ c_{51} & c_{52} & c_{53} & c_{54} & c_{55} & c_{56} \\ c_{61} & c_{62} & c_{63} & c_{64} & c_{65} & c_{66} \end{bmatrix} \quad (2.15)$$

The reduced stiffness tensor  $c_{\alpha\beta}$  is a  $6 \times 6$  symmetric tensor, whose number of independent entries can be further reduced at certain crystal symmetries. Converting the stiffness

tensor  $c_{ijkl}$  to its reduced counterpart can be easily done using the following conversion table

$ij$ or $kl$	11	22	33	23, 32	13, 31	12, 21
$\alpha$ or $\beta$	1	2	3	4	5	6

As an example, the  $c_{1231}$  has the indices  $ij = 12$  and  $kl = 31$ , and is the same value as  $c_{65}$

## 2.3 Christoffel's equation and the slowness surface

The dynamical behaviour of  $\vec{u}(\vec{r}, t)$  is described by Newton's second law

$$\rho \frac{\partial^2 \vec{u}}{\partial t^2} = \underbrace{\vec{f}(\vec{r})}_{\text{Body forces}} + \underbrace{\sum_{i,j=1}^3 \frac{\partial T_{ij}}{\partial x_j} \cdot \vec{e}_i}_{\text{Strain gradient}} \quad (2.16)$$

where  $\rho$  is the mass density and  $\vec{e}_i$  are the standard unit vectors. Body forces act on the whole body, not necessarily isotropically (e.g. gravity). For our study of waves in crystals, they are negligible. Using equations 2.8 and 2.11, and ignoring the body forces, we arrive at

$$\rho \frac{\partial^2 u_i}{\partial t^2} = \sum_{j,l,m=1}^3 c_{ijlm} \frac{\partial^2 u_m}{\partial x_j \partial x_l} \quad (2.17)$$

which resembles a wave equation. If we plug in solutions of the form

$$\vec{u}(\vec{r}, t) = U_0 \exp(i(\vec{q} \cdot \vec{r} - \omega t)) \cdot \vec{e} \quad (2.18)$$

in equation 2.17, we find the relations

$$\rho \omega^2 e_i = \sum_{j,l,m=1}^3 c_{ijlm} q_j q_l e_m \quad (2.19)$$

By defining the Christoffel Tensor with normalized wavevector components  $\hat{q}_j = \vec{q} \cdot \vec{e}_j / |\vec{q}|$

$$D_{im} = \frac{1}{\rho} \sum_{j,l=1}^3 c_{ijlm} \hat{q}_j \hat{q}_l \quad (2.20)$$

we reformulate the problem as a simple eigendecomposition of a  $3 \times 3$  symmetric matrix, which is formally known as **Christoffel's equation**

$$\sum_{i,m=1}^3 (D_{im} - v^2 \delta_{im}) e_m^o = 0 \quad (2.21)$$

The three eigenvalues  $v^2 = (\omega / |\vec{q}|)^2$  are real and correspond to the three phase velocities squared, whereas the eigenvectors  $\vec{e}^o$  with the index  $o = \{1, 2, 3\}$  correspond to the wave polarizations. We see that the phase velocity depends on the relative orientation of the crystal to the propagation direction; furthermore, although the three eigenvectors will

surely be orthogonal to each other, there is no condition requiring one of the polarizations to be parallel to the propagation direction  $\vec{q}$ ; we will call the mode with the **closest orientation to the propagation** direction as **quasi-longitudinal**, whereas the **others** will be called **quasi-transverse / quasi-shear modes**.

After sampling several orientations in the three-dimensional sphere, and for each one solving the corresponding Eigenvalue problem (equation 2.21), one can plot the angular variation of the inverse phase velocities in so called slowness-surface plots; figures 2.3, 2.4, and 2.5 show cuts over the  $x$ - and  $y$ -planes for said surfaces in Aluminum Nitride, Sapphire, and Lithium Niobate respectively. The last two materials possess trigonal symmetry, hence the similarity of the slowness surface shapes (Aluminum Nitride, on the other hand, possesses a Wurtzite crystal structure). The interpretation is simple: from the angular point of view, the radial distance corresponds to the reciprocal of a sound wave's phase velocity in the same direction, here given in units of  $(\text{km/s})^{-1}$ .

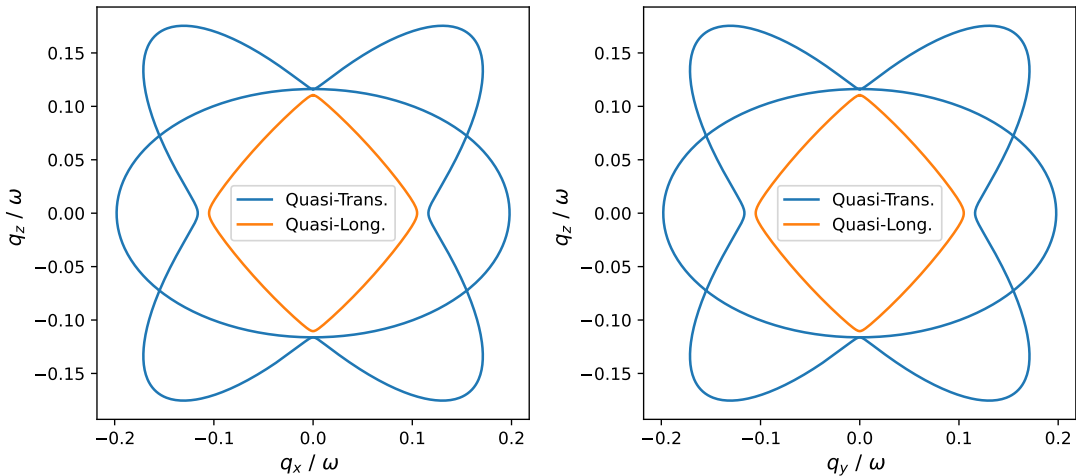


Figure 2.3: Slowness surface cuts (left:  $y$ -plane, right:  $x$ -plane) of AlN (Aluminum Nitride), in units of  $(\text{km/s})^{-1}$ . The stiffness tensor coefficients used come from [24].

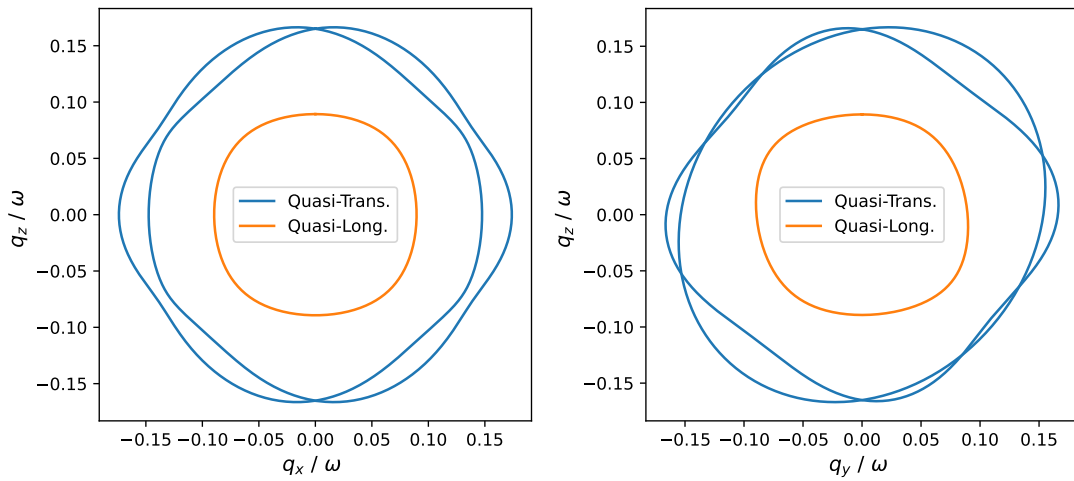


Figure 2.4: Slowness surface cuts (left:  $y$ -plane, right:  $x$ -plane) of  $\alpha - \text{Al}_2\text{O}_3$  (Sapphire), in units of  $(\text{km}/\text{s})^{-1}$ . The stiffness tensor coefficients used come from [24].

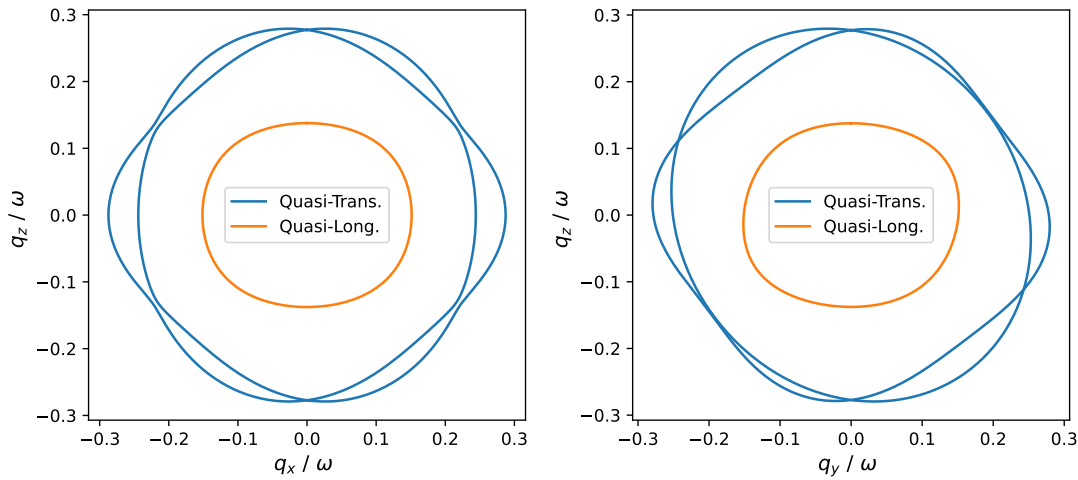


Figure 2.5: Slowness surface cuts (left:  $y$ -plane, right:  $x$ -plane) of  $\text{LiNbO}_3$  (Lithium Niobate), in units of  $(\text{km}/\text{s})^{-1}$ . The stiffness tensor coefficients used come from [24].

## Chapter 3

# High-overtone bulk acoustic resonators (HBARs)

At room temperature, high-frequency phonons (above 1 MHz) in crystalline solids exhibit a high decay rate due to intrinsic dissipation; any spatial propagation can be easily neglected. On the other hand, at low temperatures, the coherence length of phonons in a crystalline solid can be many times longer (order of meters) than the length of the solid (order of mm). The acoustic waves can propagate back and forth, reflecting off the surfaces and interfering with itself, giving rise to standing acoustic waves or modes [25]. In this thesis, we are uniquely concerned with the on-chip HBARs used in previous works [20, 26], as shown in figure 3.1. The acoustic modes are confined under the dome region, and their propagation happens predominately in  $z$ -direction (with respect to the crystal frame). We will introduce the paraxial approximations for sound waves in solids, and use them to derive important parameters, such as the stability criteria and effective horizontal velocities; the latter will be later used in the numerical simulations.

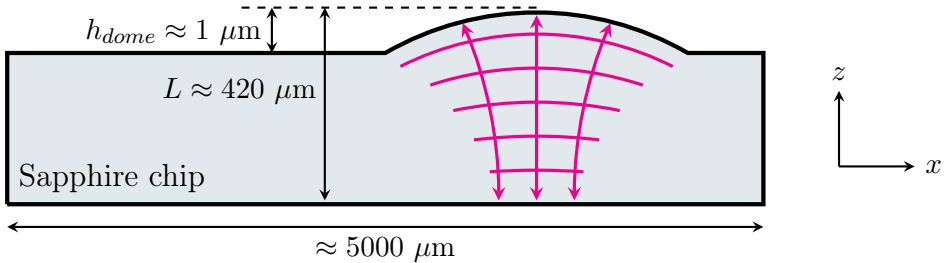


Figure 3.1: Sapphire wafers with lateral dimensions in the millimeter range and a height of  $420 \mu\text{m}$  undergo solvent reflow and reactive ion etching [27] to generate on-chip bulk acoustic resonators (HBARs). With this geometry, it is possible to confine long-coherent paraxial phononic modes (magenta lines) under the dome region. They propagate mainly in  $z$ -direction with respect to the crystal frame.

### 3.1 Paraxial wave approximations

Given that most frequency domain simulations start with an initial reciprocal space profile (or a real space profile, which is easily convertible into the former) and a given

frequency, we need a simple method to calculate  $q_z$  given  $q_x, q_y$  and  $\omega$  as parameters. However, solving equation 2.17 for a general case is a formidable task, even if one considers only one polarization. Albeit its linearity allows linear combinations of solutions and consequently Fourier decompositions, the main problem lies in the directional dependence of the phase velocity: sampling each orientation on the slowness surface requires a  $3 \times 3$  Eigendecomposition (i.e. solving equation 2.21).

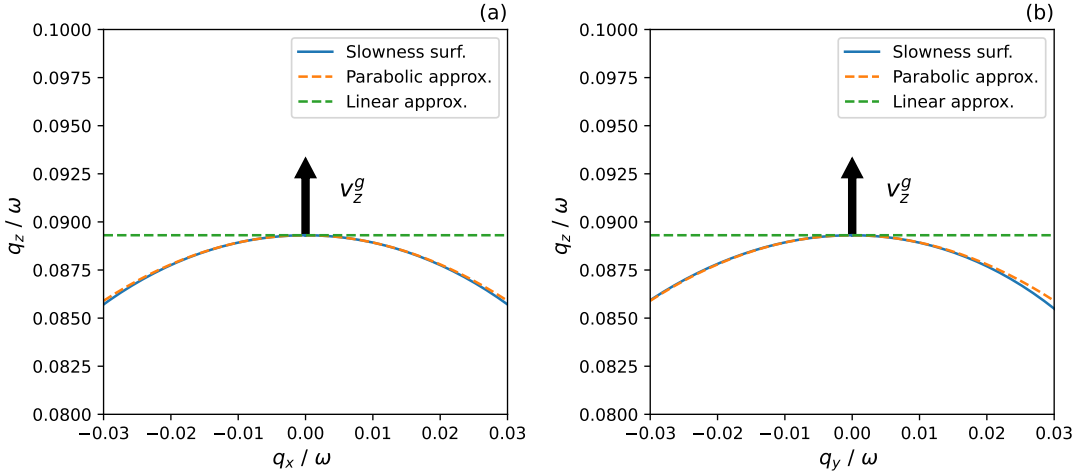


Figure 3.2: Approximating the slowness surface of Sapphire close to the point  $(q_x, q_y) = (0, 0)$ : projections in the (a)  $q_y = 0$  and (b)  $q_x = 0$  planes. The linear terms of equation 3.1 define the approximating plane, whose projections are represented as green dashed lines. The group velocity is perpendicular to the aforementioned plane.

Fortunately in HBARs, the sound beams have a narrow spatial frequency distribution and propagate mainly in the  $z$ -direction (with respect to the sample frame, see figure 3.1). We choose our Sapphire sample cuts such that the crystallographic  $z$ -axis is aligned with the sample  $z$ -axis; hence we can focus on this region of the slowness surface. One can perform a Taylor Series expansion of the slowness surface  $\mathcal{S}(\vec{q}, \omega)$  up to second order in the vicinity of the propagation direction ( $z$ -axis) [28]

$$\frac{q_z}{\omega} = S_0 + A \left( \frac{q_x}{\omega} \right) + B \left( \frac{q_y}{\omega} \right) + C \left( \frac{q_x q_y}{\omega^2} \right) + D_x \left( \frac{q_x}{\omega} \right)^2 + D_y \left( \frac{q_y}{\omega} \right)^2 + \mathcal{O}(q_x^3, q_y^3) \quad (3.1)$$

which, in essence, is the desired simple function that calculates  $q_z$  from  $q_x, q_y$  and  $\omega$ ; furthermore, it only depends on material parameters<sup>1</sup>. Figure 3.2 shows the axial projections of the slowness surface in Sapphire and its parabolic (i.e. second-order Taylor) approximation. We can give physical meaning to the parameters

- $S_0$  is the inverse phase velocity for a plane wave propagating in the  $z$ -axis

$$\vec{v}_z^{ph} = \frac{1}{S_0} \vec{\mathbf{e}}_z \quad (3.2)$$

<sup>1</sup>For our Lithium Niobate samples, we choose the cuts such that the  $y$ -axis is aligned vertically. The paraxial approximations can be derived for an arbitrary axis of propagation; we will stick to the  $z$ -axis for the following sections to avoid cumbersome notation.

- The group velocity of the central ray  $\vec{v}_z^{gr}$  can be easily calculated from the linear terms in equation 3.1 (they correspond to the linear plane shown in figure 3.2)

$$\omega = \frac{-Aq_x - Bq_y + q_z}{S_0} \quad (3.3)$$

$$\vec{v}_z^g = \left. \frac{\partial \omega}{\partial \vec{q}} \right|_{q_x, q_y=0} = \frac{1}{S_0} (-A\vec{e}_x - B\vec{e}_y + 1\vec{e}_z) \quad (3.4)$$

- $C$ ,  $D_x$  and  $D_y$  determine the curvature of paraboloid approximating the slowness surface.

Hence we reduce the problem of several eigenvalue equations to a simple quadratic function; we just need an easy method of calculating all material constants ( $S_0$ ,  $A$ ,  $B$ ,  $C$ ,  $D_x$ , and  $D_y$ ). For a general anisotropic material, unfortunately there is no useful closed form solution; one must rely on numerical approximations. In our case, derivative estimation from cubic spline interpolation [29] seems to be the only numerically stable method. Table 3.1 shows the results for some materials of interest.

	$S_0$ [m $^{-1}$ s]	$A$ [ ]	$B$ [ ]	$C$ [ms $^{-1}$ ]	$D_x$ [ms $^{-1}$ ]	$D_y$ [ms $^{-1}$ ]
Sapphire	$8.93 \cdot 10^{-5}$	$1.64 \cdot 10^{-14}$	$3.67 \cdot 10^{-9}$	$-9.41 \cdot 10^{-8}$	$-3.79 \cdot 10^3$	$-3.79 \cdot 10^3$
Quartz	$1.58 \cdot 10^{-4}$	$-1.86 \cdot 10^{-14}$	$1.15 \cdot 10^{-7}$	$-1.43 \cdot 10^{-8}$	$-4.78 \cdot 10^3$	$-4.78 \cdot 10^3$
GaAs	$2.11 \cdot 10^{-4}$	$-2.43 \cdot 10^{-14}$	$-1.39 \cdot 10^{-14}$	$1.33$	$-5.47 \cdot 10^3$	$-5.47 \cdot 10^3$
BK7	$1.65 \cdot 10^{-4}$	$-8.90 \cdot 10^{-15}$	$8.86 \cdot 10^{-15}$	$-2.62 \cdot 10^{-8}$	$-3.03 \cdot 10^3$	$-3.03 \cdot 10^3$
TiO <sub>2</sub>	$9.42 \cdot 10^{-5}$	$1.16 \cdot 10^{-14}$	$-1.21 \cdot 10^{-17}$	$6.37 \cdot 10^{-1}$	$-3.64 \cdot 10^3$	$-3.64 \cdot 10^3$
AlN	$1.10 \cdot 10^{-4}$	$2.90 \cdot 10^{-15}$	$-1.06 \cdot 10^{-14}$	$-3.63 \cdot 10^{-8}$	$-1.15 \cdot 10^5$	$-1.15 \cdot 10^5$
CaF <sub>2</sub>	$1.39 \cdot 10^{-4}$	$-1.58 \cdot 10^{-14}$	$5.26 \cdot 10^{-15}$	$-1.43 \cdot 10^{-1}$	$-1.83 \cdot 10^3$	$-1.83 \cdot 10^3$
LiNbO <sub>3</sub> *	$1.51 \cdot 10^{-4}$	$8.07 \cdot 10^{-2}$	$1.93 \cdot 10^{-14}$	$-1.78 \cdot 10^{-2}$	$-2.91 \cdot 10^3$	$-3.23 \cdot 10^3$

Table 3.1: Summary of the material constants for the quasi-longitudinal slowness surface calculated through interpolation using stiffness tensor coefficients from [24]. For most cases, we perform the Taylor approximation around the crystallographic  $z$ -axis. For LiNbO<sub>3</sub>, we approximate the  $y$ -axis, with permuted indices ( $x \rightarrow z$ ,  $y \rightarrow x$ ).

## 3.2 The effective horizontal velocity

Other simulation techniques, such as the optical Schrödinger equation (presented in section 4.2) assume an anisotropic wave equation in which every spatial derivative term has a different velocity as factor

$$\left[ v_x^2 \frac{\partial^2}{\partial x^2} + v_y^2 \frac{\partial^2}{\partial y^2} + v_z^2 \frac{\partial^2}{\partial z^2} - \frac{\partial^2}{\partial t^2} \right] u(\vec{r}, t) = 0 \quad (3.5)$$

which is equivalent to the isotropic problem with rescaled axes. Naively we could use the longitudinal phase velocities in  $x$ - and  $y$ -directions for  $v_x$  and  $v_y$ . The resulting slowness surface would be ellipsoidal in shape with its principal axes parallel to the crystal axes; however it does not necessarily match the curvature close to the axis of propagation.

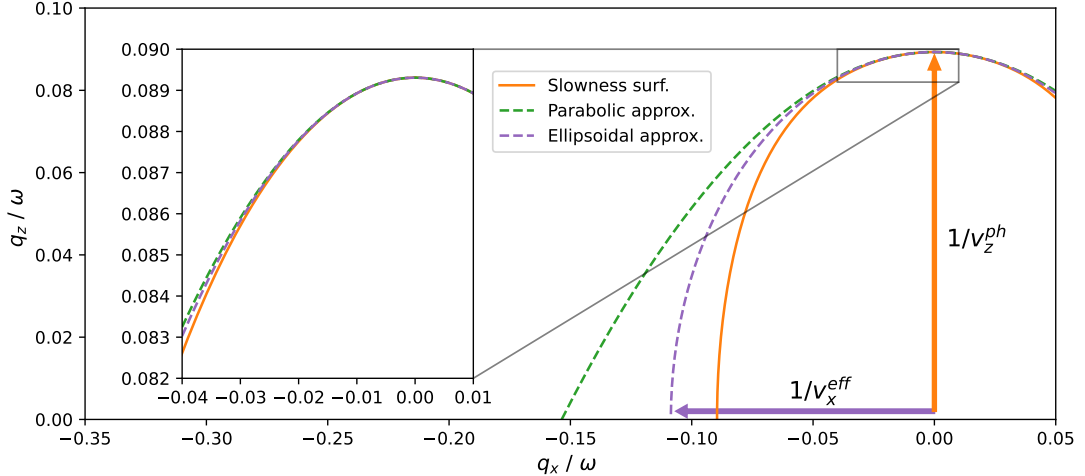


Figure 3.3: Ellipsoidal (purple) and paraboloidal (green) approximations of the slowness surface (orange) for longitudinal paraxial waves in Sapphire (all in units of  $(\text{km/s})^{-1}$ ). As one can see, they approximate the true values well at the top; however, neither the ellipse nor the parabola cross the  $q_x$  axis in the same place as the slowness surface.

Our problem can be solved if we find the corresponding ellipsoid that matches the slowness surface and its curvature around the propagation axis, as seen in figure 3.3; its principal axes lengths in  $x$ - and  $y$ -direction can be interpreted as the reciprocals of the effective horizontal velocities in  $x$ - and  $y$ -direction,  $v_x^{\text{eff}}$  and  $v_y^{\text{eff}}$  respectively. In situations where  $|C| \ll |D_x|, |D_y|$  and  $|A|, |B| \ll 1$  (which is often the case in longitudinal waves in the materials used) we can re-write equation 3.1 as

$$\frac{q_z}{\omega} = S_0 + D_x \left( \frac{q_x}{\omega} \right)^2 + D_y \left( \frac{q_y}{\omega} \right)^2 \quad (3.6)$$

which describes a centered elliptical paraboloid with the principal axes aligned to the Cartesian axes. We then perform an ellipsoidal approximation on top of the paraboloidal. Starting from the general equation describing an ellipsoid,

$$\frac{1}{a^2} \left( \frac{q_x}{\omega} \right)^2 + \frac{1}{b^2} \left( \frac{q_y}{\omega} \right)^2 + \frac{1}{c^2} \left( \frac{q_z}{\omega} \right)^2 = 1 \quad (3.7)$$

with  $a$ ,  $b$  and  $c$  representing the radii along each of the principal axes, we equate the zeroth and second derivatives

$$\frac{q_z}{\omega} = c \sqrt{1 - \frac{1}{a^2} \left( \frac{q_x}{\omega} \right)^2 - \frac{1}{b^2} \left( \frac{q_y}{\omega} \right)^2} \quad (3.8)$$

$$\approx c - \frac{c}{2a^2} \left( \frac{q_x}{\omega} \right)^2 - \frac{c}{2b^2} \left( \frac{q_y}{\omega} \right)^2 \quad (3.9)$$

$$\implies c = S_0 \quad (3.10)$$

$$\implies a^2 = -\frac{S_0}{2D_x} = -\frac{1}{2D_x v_z^{\text{ph}}} \quad (3.11)$$

$$\implies b^2 = -\frac{S_0}{2D_y} = -\frac{1}{2D_y v_z^{\text{ph}}} \quad (3.12)$$

where  $v_z^{ph} = (S_0)^{-1}$  is the phase velocity for waves in  $z$ -direction. Hence, we define the **effective horizontal velocities**:

$$v_x^{eff} = \frac{1}{a} = \sqrt{-2D_x v_z^{ph}} = \sqrt{-\frac{2D_x}{S_0}} \quad (3.13)$$

$$v_y^{eff} = \frac{1}{b} = \sqrt{-2D_y v_z^{ph}} = \sqrt{-\frac{2D_y}{S_0}} \quad (3.14)$$

Hence, we see that, for paraxial waves close to the  $q_z$ -axis, the horizontal components behave as if the solid had horizontal velocities in  $v_x^{eff}$  and  $v_y^{eff}$ ; these effective velocities **do not necessarily** correspond to the true phase velocities, as seen in figure 3.3 and table 3.2; the latter summarizes the effective horizontal velocities calculated from the paraxial parameters in table 3.1. Coincidentally, in all materials of interest,  $v_x^{eff}$  and  $v_y^{eff}$  are equal.

### 3.3 Stability criteria

Not surprisingly, acoustic modes in a solid suffer from diffraction losses (see figure 3.4a for an unconfined mode); however, much like using curved mirrors to confine light in a laser cavity, the boundaries of crystalline medium can be shaped to confine these longitudinal acoustic modes, as shown in figure 3.4b.

The spectrum of standing-wave modes for a crystalline medium depends on the geometry (i.e. the shape of boundaries) and also on the orientation and anisotropy of the crystal. Similar to paraxial Gaussian photonic beams in Fabry-Pérot resonators [30], we do not have complete freedom in the choice of shapes; the sound waves must fulfill the stability criteria<sup>2</sup> [27, 28]

$$0 \leq \left(1 - \frac{L}{\chi_x R_1}\right) \left(1 - \frac{L}{\chi_x R_2}\right) \leq 1 \quad (3.15)$$

$$0 \leq \left(1 - \frac{L}{\chi_y R_1}\right) \left(1 - \frac{L}{\chi_y R_2}\right) \leq 1 \quad (3.16)$$

where  $R_1$  and  $R_2$  are radii of curvature of the mirrors,  $L$  is the distance between the mirrors and  $\chi_x, \chi_y$  are the anisotropy parameters [28]. In the simple case discussed in section 3.2, these are given as:

$$\chi_x = -2D_x S_0 = \left(\frac{v_x^{eff}}{v_z^{ph}}\right)^2 \quad (3.17)$$

$$\chi_y = -2D_y S_0 = \left(\frac{v_y^{eff}}{v_z^{ph}}\right)^2 \quad (3.18)$$

The anisotropy parameters are correction factors arising from the different axial velocities of paraxial waves in solids; they rescale the dimensions of the isotropic solid problem such that it matches the anisotropic case.

---

<sup>2</sup>The stability criteria come from a laborious derivation, which consists in fitting Gaussian, Laguerre-Gaussian and Hermitian-Gaussian modes such that the radii of curvature of both left and right wavefronts match the resonators' mirrors. There is no general analytical solution; we refer to the supplemental material of [27] for an analytic derivation of materials with cubic symmetry and [28] for a more general derivation using the paraxial material constants.

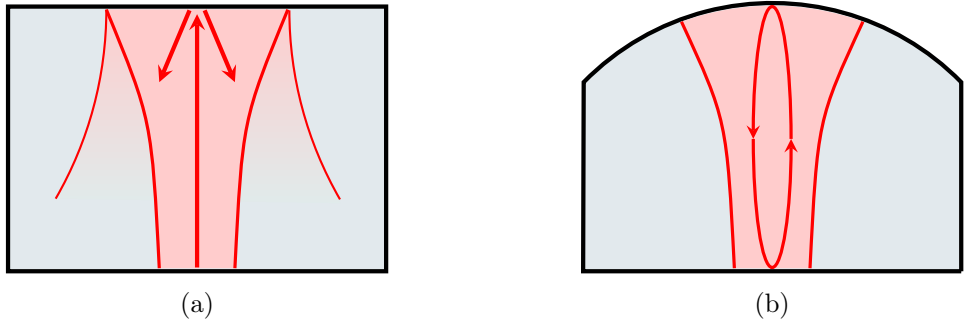


Figure 3.4: Bulk acoustic resonators in (a) plano-plano geometry and (b) plano-convex geometry. The latter configuration confines the modes in the horizontal direction. Adapted from [25].

Equations 3.15 and 3.16 guarantee mode confinement in the respective axes. The plano-convex architecture in figure 3.4b corresponds to the limit  $R_1 \rightarrow \infty$ , and the stability criteria become:

$$0 \leq \left(1 - \frac{L}{\chi_x R_2}\right) \leq 1 \implies \chi_x R_2 \geq L \quad (3.19)$$

$$0 \leq \left(1 - \frac{L}{\chi_y R_2}\right) \leq 1 \implies \chi_y R_2 \geq L \quad (3.20)$$

Typical values for  $\chi$  are shown in table 3.2. Given that most materials of interest have a  $\chi > 0.5$ , and we work with samples whose thickness  $L \approx 420 \mu\text{m}$ , we can set a safe boundary of minimal radius of curvature of  $R_{min} = 1000 \mu\text{m} = 1 \text{ mm}$ .

	$v_x^{ph}$	$v_x^{eff}, v_y^{eff}$	$v_z^{ph}$	$\chi_x, \chi_y$
Sapphire	$1.116 \cdot 10^4$	$9.208 \cdot 10^3$	$1.120 \cdot 10^4$	0.68
Quartz	$5.718 \cdot 10^3$	$7.782 \cdot 10^3$	$6.338 \cdot 10^3$	1.51
GaAs	$4.731 \cdot 10^3$	$7.196 \cdot 10^3$	$4.731 \cdot 10^3$	2.31
BK7	$6.064 \cdot 10^3$	$6.064 \cdot 10^3$	$6.064 \cdot 10^3$	1.00
TiO <sub>2</sub>	$7.946 \cdot 10^3$	$8.785 \cdot 10^3$	$1.061 \cdot 10^4$	0.68
AlN	$9.536 \cdot 10^3$	$4.556 \cdot 10^4$	$9.057 \cdot 10^3$	25.31
CaF <sub>2</sub>	$7.204 \cdot 10^3$	$5.134 \cdot 10^3$	$7.204 \cdot 10^3$	0.51

Table 3.2: Summary of the true longitudinal horizontal velocities  $v_x^{ph}$ , effective horizontal velocities  $v_x^{eff}$ , longitudinal velocities in  $z$ -direction  $v_z^{ph}$  and anisotropy parameters, all calculated from the material constants in table 3.1. All velocities in (m/s). For most materials of interest,  $v_x^{eff}$  and  $v_y^{eff}$  are equal, which implies that  $\chi_x = \chi_y$ . The ellipsoidal approximation breaks down for LiNbO<sub>3</sub>, since  $D_x$  and  $D_y$  are **not** equal and the linear coefficient  $A$  is **not** negligible (in fact it is  $10^{10}$  times bigger than see table 3.1), which would correspond to a non-centered ellipsoid and give different velocities for waves propagating forwards and backwards, effectively breaking time reversal symmetry; hence its absence from this table.

# Chapter 4

## Numerical simulations

From subsection 3.3 we are guaranteed the existence of standing phononic modes inside the crystal, provided its geometry fullfills the stability criteria. We are interested in calculating the frequencies and spatial profiles of the aforementioned modes. We will look at two different approaches: frequency domain simulations that probe the response of a harmonic input field and the optical Schrödinger equation, which allows us to predict the effects of marginal changes to the dome shapes.

### 4.1 Frequency domain simulations (BeamProp)

Considering an acoustic field  $\vec{\mathbf{u}}(x, y, z, t)$  propagating in the  $z$  direction, we can follow the approach in [28] and decompose into its plane wave basis components

$$\vec{\mathbf{u}}(x, y, z, t) = \sum_{n=1}^3 \left(\frac{1}{2\pi}\right)^3 \int_{\mathbb{R}} d\omega \int_{\mathbb{R}^2} dq_x dq_y \phi^n(q_x, q_y, \omega) \cdot \vec{\mathbf{d}}^n \left(\frac{q_x}{\omega}, \frac{q_y}{\omega}\right) e^{i(\omega t - q_x x - q_y y - q_z^n z)} \quad (4.1)$$

where  $n = \{1, 2, 3\}$  indexes the three slowness surfaces,  $\vec{\mathbf{d}}^n(q_x/\omega, q_y/\omega)$  is the polarization vector for the plane wave propagating along  $(q_x, q_y, q_z^n)$ ,  $q_z^n$  is determined using interpolated values from the true slowness surface and  $\phi^n(q_x, q_y, \omega)$  corresponds to the amplitude for each polarization. Supposing the displacement is known at an initial plane  $\vec{\mathbf{u}}(x, y, z = 0, t)$ , we can take the inverse Fourier transform and obtain

$$\sum_{i=1}^3 \phi^i(q_x, q_y, \omega) \cdot \vec{\mathbf{d}}^i \left(\frac{q_x}{\omega}, \frac{q_y}{\omega}\right) = \vec{\mathbf{H}}(q_x, q_y, \omega, z = 0) \quad (4.2)$$

$$\vec{\mathbf{H}}(q_x, q_y, \omega, z = 0) = \int_{\mathbb{R}} dt \int_{\mathbb{R}^2} dx dy \vec{\mathbf{u}}(x, y, 0, t) e^{i(-\omega t + q_x x + q_y y)} \quad (4.3)$$

the two dimensional Fourier transform of the input field. Whereas for a given propagation direction the vectors  $\vec{\mathbf{d}}^i$  are orthogonal, specification of  $q_x$  and  $q_y$  give them different values for  $q_z$ , which results in generally different propagation directions, hence we **cannot** assume the polarizations to be orthogonal to each other. Projecting equation 4.3 onto

these unit vectors gives the general solution

$$F_{11} = \vec{\mathbf{H}} \cdot \vec{\mathbf{d}}^1 \left[ 1 - (\vec{\mathbf{d}}^2 \cdot \vec{\mathbf{d}}^3)^2 \right] \quad (4.4)$$

$$F_{12} = \vec{\mathbf{H}} \cdot \vec{\mathbf{d}}^2 \left[ (\vec{\mathbf{d}}^1 \cdot \vec{\mathbf{d}}^3)(\vec{\mathbf{d}}^2 \cdot \vec{\mathbf{d}}^3) - (\vec{\mathbf{d}}^2 \cdot \vec{\mathbf{d}}^3) \right] \quad (4.5)$$

$$F_{13} = \vec{\mathbf{H}} \cdot \vec{\mathbf{d}}^3 \left[ (\vec{\mathbf{d}}^1 \cdot \vec{\mathbf{d}}^2)(\vec{\mathbf{d}}^2 \cdot \vec{\mathbf{d}}^3) - (\vec{\mathbf{d}}^1 \cdot \vec{\mathbf{d}}^3) \right] \quad (4.6)$$

$$\phi^1 = \frac{F_{11} + F_{12} + F_{13}}{1 + 2(\vec{\mathbf{d}}^1 \cdot \vec{\mathbf{d}}^2)(\vec{\mathbf{d}}^1 \cdot \vec{\mathbf{d}}^3)(\vec{\mathbf{d}}^2 \cdot \vec{\mathbf{d}}^3) - (\vec{\mathbf{d}}^1 \cdot \vec{\mathbf{d}}^2)^2 - (\vec{\mathbf{d}}^1 \cdot \vec{\mathbf{d}}^3)^2 - (\vec{\mathbf{d}}^2 \cdot \vec{\mathbf{d}}^3)^2} \quad (4.7)$$

with the solutions for  $\phi^2$  and  $\phi^3$  obtained by index permutation. With the components determined, we can focus on simulating the bulk acoustic resonators (BARs).



Figure 4.1: Graphical representation of the BeamProp algorithm. Magenta arrows represent steps happening in reciprocal space, whereas black ones represent steps in real space. The numbers indicate the step numbers shown below (1. Input field, 2. Forward propagation in reciprocal space, 3. Position-dependent geometrical factor  $\varphi_{gm}$ , which depends on the height profile of the dome  $h(x, y)$ , 4. Backward propagation in reciprocal space, and 5. Combining input with propagated field).

Our simulator, BeamProp, is based on previous work [25, 31], with some extra features; the algorithm is based on propagating acoustic beams back and forth along the crystal and looking for the stable solutions (see figure 4.1 for a comprehensive diagram)

1. Start with an harmonic input field (assuming we have only one polarization)

$$\vec{\mathbf{u}}^0(x, y, z = 0) \exp(i\omega t). \quad (4.8)$$

2. Map the spatial profile into its corresponding Fourier transform

$$\vec{\mathbf{H}}^0(q_x, q_y, \omega, z = 0) = \int_{\mathbb{R}^2} dx dy \vec{\mathbf{u}}^0(x, y, 0, t) e^{i(q_x x + q_y y)} \quad (4.9)$$

and propagate each polarization over the length of the resonator  $L$  at reciprocal space

$$\vec{\mathbf{H}}^0(q_x, q_y, \omega, z = L) = \vec{\mathbf{H}}^0(q_x, q_y, \omega, z = 0) \cdot \exp(-iL \cdot q_z(q_x, q_y, \omega)) \quad (4.10)$$

where  $q_z(q_x, q_y, \omega)$  can be either the quadratic approximation or the interpolated slowness surface.

3. Return to the real space profile via inverse Fourier transformation

$$\vec{\mathbf{u}}^0(x, y, z = L) = \left(\frac{1}{2\pi}\right)^2 \int_{\mathbb{R}^2} dq_x dq_y \vec{\mathbf{H}}^0(q_x, q_y, \omega, z = L) e^{-i(q_x x + q_y y)} \quad (4.11)$$

and apply a position-dependent phase shift  $\varphi_{gm}$  (which corresponds to the beam propagating inside the curved surface and back) in real space

$$\vec{\mathbf{u}}^{0,p}(x, y, z = L) = \vec{\mathbf{u}}^0(x, y, z = L) \cdot \exp(-i\varphi_{gm}) \quad (4.12)$$

$$\varphi_{gm} = 2 \cdot q_z(0, 0, \omega) \cdot h(x, y). \quad (4.13)$$

The surface can have an arbitrary shape, which is captured as a height profile  $h(x, y)$ . The factor 2 means the sound wave propagates forwards, is reflected on a free surface (i.e. no stress, hence no extra phase). Simply adding a position-dependent phase with a constant wavevector neglects the slowness surface dispersion and the different propagation directions for each spatial Fourier component. Nevertheless, we are only considering paraxial waves, which means that all Fourier components have  $q_x, q_y \ll q_z$ , justifying the approximation.

4. Map the post-surface-reflected field  $\vec{\mathbf{u}}^{0,p}(x, y, L, t)$  to its Fourier transform

$$\vec{\mathbf{H}}^{0,p}(q_x, q_y, \omega, z = L) = \int_{\mathbb{R}^2} dx dy \vec{\mathbf{u}}^{0,p}(x, y, L, t) e^{i(q_x x + q_y y)} \quad (4.14)$$

and propagate the wave back to the left surface

$$\vec{\mathbf{H}}^{0,p}(q_x, q_y, \omega, z = 0) = \vec{\mathbf{H}}^{0,p}(q_x, q_y, \omega, z = L) \cdot \exp(-iL \cdot q_z(q_x, q_y, \omega)). \quad (4.15)$$

5. Return to the real space profile via inverse Fourier transformation,

$$\vec{\mathbf{u}}^{0,p}(x, y, z = 0) = \left(\frac{1}{2\pi}\right)^2 \int_{\mathbb{R}^2} dq_x dq_y \vec{\mathbf{H}}^{0,p}(q_x, q_y, \omega, z = 0) e^{-i(q_x x + q_y y)}. \quad (4.16)$$

Similar to step 3, we could add a surface phase corresponding to a height profile on the left surface and effectively simulate convex-convex geometries with different dome shapes; they are beyond the scope of this project. We add the resulting field to the harmonic input field

$$\vec{\mathbf{u}}^1(x, y, z = 0) = \vec{\mathbf{u}}^0(x, y, z = 0) + \vec{\mathbf{u}}^{0,p}(x, y, z = 0) \quad (4.17)$$

6. Repeat steps 2 to 5 for  $m$  times, increasing the index at each iteration

$$\vec{\mathbf{u}}^2(x, y, z = 0) = \vec{\mathbf{u}}^0(x, y, z = 0) + \vec{\mathbf{u}}^{1,p}(x, y, z = 0) \quad (4.18)$$

$$\vdots \quad (4.19)$$

$$\vec{\mathbf{u}}^m(x, y, z = 0) = \vec{\mathbf{u}}^0(x, y, z = 0) + \vec{\mathbf{u}}^{m-1,p}(x, y, z = 0). \quad (4.20)$$

7. Calculate the intensity of the field

$$I(\omega) = \int_{\mathbb{R}^2} dx dy |\vec{\mathbf{u}}^m|^2. \quad (4.21)$$

For non-resonant fields, step 6 adds spatial profiles with different phases, which on average will interfere randomly. On the other hand, for resonant fields, each round trip adds a phase multiple of  $2\pi$ . Hence, step 6 adds spatial profiles with matching phases, which results in a maximized integral  $I(\omega)$ . We can perform a frequency sweep over several frequencies, and the resonant fields will appear as peaks in the mechanical resonance spectrum (i.e. a plot of  $I(\omega)$ ).

8. As soon as a resonance frequency  $\Omega_r$  is found, the output field from the last iteration  $\vec{u}^m(x, y, z = 0)$  is propagated for further round-trips. After several iterations, the spatial profile converges to the mode profiles of the standing wave acoustic modes.

Some notes regarding the algorithm:

- It is mathematically easier to perform one single real-space convolution instead of going to reciprocal space, propagating the beam there, and returning to real space for a one-way trip inside the resonator. However, for most computational purposes, the Fast Fourier Transform and its inverse are so efficiently implemented, they outperform the simpler operation.
- The reason we first perform the sweep in the frequency  $\omega$  and then perform further sweeps in the resonance frequencies  $\Omega_i$  has to do with computational efficiency: on the first sweep, we only need to distinguish the peaks in the resonance spectrum (usually 100 round trips suffice). For the spatial profile of the modes, we need convergence of the spatial profile of the mode; the latter condition requires at least 500 roundtrips for acceptable results. For the results presented we are using 200 roundtrips for frequency sweeps and 1000 for resonant mode profile calculations.

From previous work [25], we know that for  $z$ -polarized, gaussian input fields

$$\vec{u}^0(x, y, z = 0) \propto \exp\left(-\frac{x^2 + y^2}{2\sigma^2}\right) \vec{e}_z \quad (4.22)$$

less than 2% of the power gets transferred to other polarizations; hence, we can safely assume the mode is purely longitudinal and only propagate its component back and forth, thereby reducing the necessary calculations by a factor of three.

#### 4.1.1 Adding a secondary material layer

Recent experiments use domes with piezoelectric materials for increased electromechanical couplings [26]; we wish to incorporate a variable piezoelectric thickness (of the order of 1 um, smaller than the dome height) to each of our dome shapes. We only need to modify step 3 of the BeamProp, namely the surface dependent phase shift. Interfaces add two elements to the simulation: refraction and reflection due to the different velocities. The first one can be easily incorporated by reinterpreting the problem: the geometrical phase shift  $\varphi_{gm}$  is given by

$$\varphi_{gm} = 2 \cdot q_z(0, 0, \omega) \cdot h(x, y) = 2 \cdot \left( \frac{\omega}{v_{l,z}^0} h_0(x, y) + \frac{\omega}{v_{l,z}^p} h_p(x, y) \right) \quad (4.23)$$

where  $v_{l,z}^0$  and  $v_{l,z}^p$  are the longitudinal phase velocities in  $z$ -direction inside the bulk material and piezoelectric layer, and  $h_0(x, y)$  and  $h_p(x, y)$  are the height profile of the

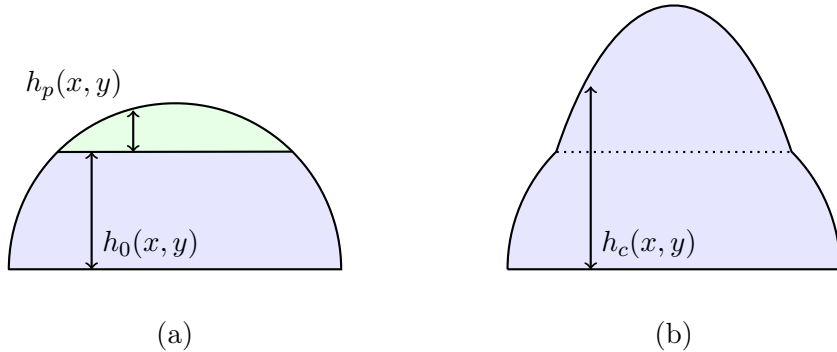


Figure 4.2: Simulating heterogeneous domes by a) considering both materials, with different thicknesses and velocities and b) by rescaling the piezoelectric layer by a factor of  $v_{l,z}^0/v_{l,z}^p$  which yields an equivalent solution (in this case, the piezoelectric layer has a smaller longitudinal velocity, which results in a bigger dome).

material and piezoelectric layer, respectively (as shown in figure 4.2). Instead of simulating two different materials, we can simply rearrange the terms in equation 4.23

$$\varphi_{gm} = 2 \cdot \left( \frac{\omega}{v_{l,z}^0} h_0(x, y) + \frac{\omega}{v_{l,z}^p} h_p(x, y) \right) \quad (4.24)$$

$$= 2 \cdot \left( \frac{\omega}{v_{l,z}^0} h_0(x,y) + \underbrace{\frac{\omega}{v_{l,z}^0} \frac{v_{l,z}^0}{v_{l,z}^p} \cdot h_p(x,y)}_{=h_p^{eff}(x,y)} \right) \quad (4.25)$$

$$= 2 \frac{\omega}{v_{l,z}^0} \cdot \left( h_0(x,y) + h_p^{eff}(x,y) \right) \quad (4.26)$$

$$= 2 \frac{\omega}{v_{l,z}^0} h_c(x, y) = 2 q_z(0, 0, \omega) \cdot h_c(x, y) \quad (4.27)$$

and we see that rescaling the piezolayer by the ratio of the sound velocities yields an effective piezo thickness  $h_p^{eff}(x, y) = v_{l,z}^0 \cdot h_p(x, y)/v_{l,z}^p$  and an equivalent phase shift.

### 4.1.2 Limitations

The BeamProp simulations have three main limitations:

- **Acoustic impedance mismatch:** if both materials have a different acoustic impedance, we can no longer assume perfect transmission at the interface; each incident wave should be decomposed into transmitted and reflected. Furthermore, the reflection and transmission coefficients are dependent on the angle of incidence. For a rough estimate, the acoustic impedance for planar longitudinal waves in  $z$ -direction is

$$Z = \rho v_{l,z} \quad (4.28)$$

namely the product of its density and phase velocity. The reflection coefficient for an heterogeneous interface, with a wave travelling from material 1 to material 2 is

$$R = \frac{Z_2 - Z_1}{Z_1 + Z_2} \quad (4.29)$$

BeamProp does not calculate any surface reflections, essentially assuming perfect transmission. A rough estimate using values from [24] for Sapphire-AlN and Sapphire-LiNbO<sub>3</sub> interfaces gives us reflection coefficients of 0.19 and 0.20, respectively.

- **Slowness surface at the dome:** beam propagations inside the dome are performed with the 0-th order approximation of the slowness surface

$$q_z(q_x, q_y, \omega) = q_z(0, 0, \omega) \quad (4.30)$$

In the case of paraxial beams, the condition  $q_x, q_y \ll q_z$  holds. Together with the fact that the slowness surface is continuous, the approximation is justified.

- **Computationally expensive:** Each simulation (frequency sweep and spatial profile estimation) has a runtime of 3 to 4 minutes. It does not offer any physical intuition to how the Eigenstates might be modified under a parametrical change, e.g. the radius of curvature or dome height.

Fortunately we have other ways of predicting marginal changes; they are introduced in section 4.2.

#### 4.1.3 Implementation and performance analysis

The code is implemented as a software library in Python. New features added from the legacy codebase include:

- **Arbitrary choice of materials:** we can now pair any material with any piezo layer on the surface. The user is only required to save the stiffness tensor, density, and specify the crystal orientation. The slowness surface is calculated (with the Christoffel library [32]) and the paraxial material constants are obtained. The current version uses all material constants from [24].
- **Arbitrary choice of dome shapes:** we can now simulate any dome shape by simply specifying the shape as a two-dimensional function.

The discretized spatial profile of the mode is implemented as a two-dimensional Numpy array, which allows us to use the FFT submodule to implement the fourier transformations efficiently [33]. For each roundtrip, and assuming a  $n \times n$  array, the algorithmic cost can be summarized as:

- Phase and surface multiplications:  $\mathcal{O}(n^2)$ .
- Two-dimensional discrete Fourier transforms (DFTs):  $\mathcal{O}(n^2 \log(n^2))$ .

which, for a frequency sweep of  $N_f$  frequency points and each for  $N_R$  roundtrips gives us an overall cost of  $\mathcal{O}(N_f \cdot N_R \cdot n^2 \log(n^2))$ . In order to leverage the multi-core architecture of current computers, we consider two different strategies:

- **Parallelize the DFTs:** Some Python libraries, such as PyFFTW [34], offer parallelized versions of the DFTs.
- **Parallelize the frequency sweep:** For frequency point in a frequency sweep, BeamProp performs several roundtrips. Given that each the results among these frequency points are completely independent of each other, we can perform them in parallel using the concurrent.futures module included in the standard library.

PyFFTW does offer a significant speedup compared to the numpy fft module for large matrices, provided the user compiles the underlying FFTW library [35] with the correct flags. Since we are targeting different operating systems and architectures, and wish to have minimal effort on the installation, this option is not suitable.

The concurrent.futures module, is included in the Python standard library [36], and automatically manages the pool of subprocesses such that all cores are used for the computations. It employs data parallelism, i.e. it copies all the required resources to the subprocesses. This strategy completely avoids any deadlocks from shared-memory parallelism and does not require communication between the subprocesses during the execution (other than the initial copying of data and returning the result); nevertheless, it multiplies the memory requirements by the factor of cores available. In order to reduce the memory footprint, we implemented the algorithm as a pure global function whose arguments include the input field  $\vec{u}^0$ , the dome surface profile  $h(x, y)$  and the reciprocal space meshing, among other constants that add little overhead. A helpful diagram is shown in figure 4.3.

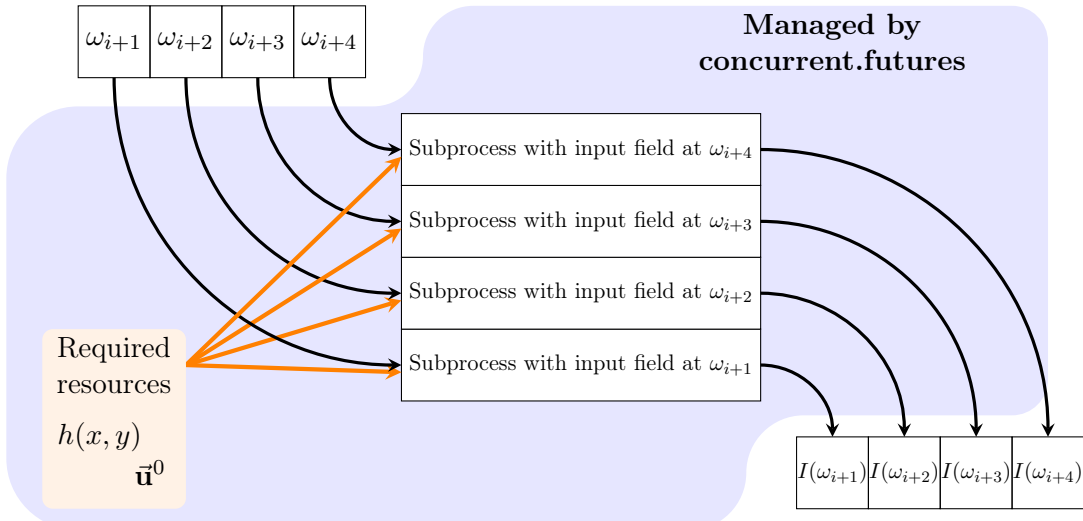


Figure 4.3: Strategy for the parallelization on the frequency sweep. The concurrent.futures module creates a pool of workers and feeds them the input frequency  $\omega_i$  and local copies of the required resources, such as the input field  $\vec{u}^0$  and the dome surface profile  $h(x, y)$ . Each worker runs a subprocess with its own independent memory and runs concurrently with and independently of the others. After  $N_R$  roundtrips, the intensity of the mode profile,  $I(\omega_i)$ , is calculated (step 7 in the BeamProp algorithm). The subprocess returns  $I(\omega_i)$  to the main process, which stores in the corresponding position in a separate array; the subprocess is terminated and its resources deleted. The concurrent.futures notices a free worker and feeds it the next element in the frequency array and the corresponding required resources.

For a spatial meshing of  $128 \times 128$  entries, each subprocess used between 100 MB and 200 MB of memory, with a speedup close to the number of cores. Further testing on three different operating systems yielded similar results.

## 4.2 Optical Schrödinger Equation (OSE) simulations

Whereas the frequency domain simulations take into account several physical factors, it is advantageous to have a simpler method for predicting marginal changes. The key concept is the similarity between the paraxial wave equation and the Schrödinger equation. Following the approach from [37, 38], we generalize the Helmholtz wave equation to an anisotropic case:

$$\left[ v_t^2(x, y) \underbrace{\left( \frac{\partial^2}{\partial x^2} + \frac{\partial^2}{\partial y^2} \right)}_{\nabla_\perp^2} + v_l^2(x, y) \frac{\partial^2}{\partial z^2} - \frac{\partial^2}{\partial t^2} \right] u = 0 \quad (4.31)$$

where the wave velocities depend on direction and position:

$$v_l(x, y) = \frac{v_{l,0}}{n(x, y)} \quad v_t(x, y) = \frac{v_{t,0}}{n(x, y)} \quad \omega = v_{l,0}q \quad (4.32)$$

which is conceptually equivalent to a spatially varying index of refraction  $n(x, y)$ . In the previous equation,  $v_{l,0}$  is the phase velocity in  $z$ -direction, and  $v_{t,0}$  is the effective horizontal velocity introduced in section 3.1. We will also assume

$$\frac{\partial n(x, y)}{\partial x} \approx \frac{\partial n(x, y)}{\partial y} \approx 0, \quad 1 - n^2(x, y) \ll 1. \quad (4.33)$$

We are looking for solutions of the form

$$u_z(\vec{r}, t, q) = u_0(\vec{r}) \exp(i(qz - \omega t)) \quad (4.34)$$

where  $u_0(\vec{r})$  is a slowly varying function in  $z$  direction. Inserting this Ansatz in 4.31, one obtains

$$v_t^2(x, y) \nabla_\perp^2 u_0 + \underbrace{v_l^2(x, y) \frac{\partial^2 u_0}{\partial z^2}}_{=0} + 2iq v_l^2(x, y) \frac{\partial u_0}{\partial z} - v_l^2(x, y) q^2 u_0 + \omega^2 u_0 = 0 \quad (4.35)$$

$$\frac{v_t^2(x, y)}{2q^2 v_l^2(x, y)} \nabla_\perp^2 u_0 + \frac{i}{q} \frac{\partial u_0}{\partial z} - \frac{1}{2} \left[ 1 - \frac{\omega^2}{q^2 v_l^2(x, y)} \right] u_0 = 0 \quad (4.36)$$

$$\frac{i}{q} \frac{\partial u_0}{\partial z} = -\frac{1}{2q^2} \frac{v_t^2}{v_{l,0}^2} \nabla_\perp^2 u_0 + \frac{1}{2} \left[ 1 - n^2(x, y) \right] u_0. \quad (4.37)$$

The key concept here is to perform a suitable change of variable; we define the equivalent time

$$\tau = q \cdot z \quad (4.38)$$

which corresponds to the phase gained by travelling a distance  $z$ ; after some careful substitutions, one obtains from equation 4.37

$$i \frac{\partial}{\partial \tau} u_0(x, y, \tau) = \left[ -\frac{1}{2q^2} \frac{v_t^2}{v_{l,0}^2} \nabla_\perp^2 + \frac{1}{2} (1 - n^2(x, y)) \right] u_0(x, y, \tau). \quad (4.39)$$

Equation 4.39 is a time-dependent Schrödinger equation (with  $\hbar = 1$ ) of a hypothetical particle with mass  $m^* = q^2 v_{l,0}^2 / v_t^2 = \omega^2 / v_t^2$  under the potential  $V(x, y) = [1 - n^2(x, y)]/2$ .

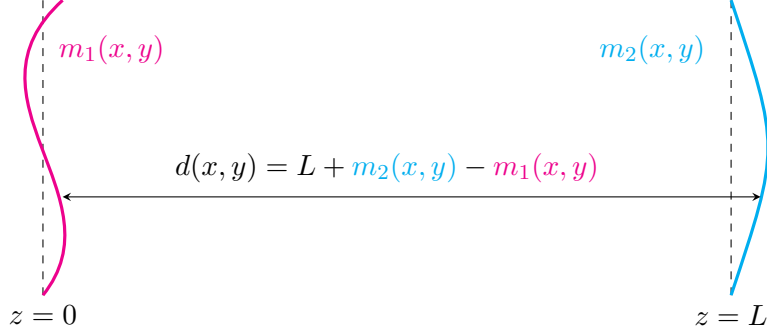


Figure 4.4: Resonator with height profiles  $m_1(x, y)$  and  $m_2(x, y)$ . The parallel distance is given by  $d(x, y) = L + m_2(x, y) - m_1(x, y)$ .

Consider now a Fabry-Pérot resonator in which the mirrors are not perfectly flat, but are described by the height profiles  $m_1(x, y)$  and  $m_2(x, y)$ . Each indicates the height deviation from the planar mirror, as shown in figure 4.4. The phase picked up in a one-way trip is

$$\varphi(x, y) = qd(x, y) \quad (4.40)$$

$$= q(L + m_2(x, y) - m_1(x, y)) \quad (4.41)$$

$$= qL \underbrace{\left( 1 + \frac{m_2(x, y) - m_1(x, y)}{L} \right)}_{n(x, y)} \quad (4.42)$$

where we re-interpret the problem as a planar resonator with a spatially varying index of refraction  $n(x, y)$ . The constraints in equation 4.33 imply  $m_i(x, y) \ll L \ i \in \{1, 2\}$ . Since the phase depends only on the difference of the height profiles,  $m_2(x, y) - m_1(x, y)$ , we can easily model convex-convex geometries of different dome shapes on each side, and by using the same trick on section 4.1.1, we can also model domes with a piezoelectric layer on the top.

Let us now consider solutions where we can apply a separation of space and time dependency, as is common in solutions to the time-dependent Schrödinger equation

$$\left[ -\frac{1}{2m^*} \nabla_\perp^2 + \frac{1}{2} (1 - n^2(x, y)) \right] u_\eta(x, y) = \eta u_\eta(x, y) \quad u_0(x, y, \tau) = e^{-i\eta\tau} u_\eta(x, y) \quad (4.43)$$

The mode function  $u_0(\vec{r})$  of the Ansatz in equation 4.34 picks up a phase as the wave travels through the resonator; it corresponds to the Gouy phase shift. The total phase (mode function and exponential part) gained in a round trip is

$$\Delta\varphi = 2qn_0(1 - \eta)L = 2\pi m \quad m \in \mathbb{N} \quad (4.44)$$

where  $n_0 = n(0, 0)$  and the last condition is required for constructive self interference<sup>1</sup>. The free spectral range and the frequencies are

$$FSR = \frac{v_{l,0}}{2n_0L} \quad f = \frac{m \cdot FSR}{1 - \eta} \stackrel{|\eta| \ll 1}{\approx} m \cdot FSR \cdot (1 + \eta). \quad (4.45)$$

<sup>1</sup>We could have picked any point in the dome, as the stability conditions require the wavefronts to match the mirrors on each side. To be consistent here, and to be sure we are inside the dome regardless of its size, we pick the point  $(x, y) = (0, 0)$

In summary each Eigenstate has both a major and minor energy component, characterized by the integer  $m$  and the real eigenvalues  $\eta$  respectively. For a pure Sapphire HBAR of length  $n_0 L = 420 \mu\text{m}$ , we have an  $FSR \approx 13.3 \text{ MHz}$ . The physical interpretation of these parameters will become clear in the following example.

### Circular domes and quantum harmonic oscillators

Considering a more practical example of circular dome of radius of curvature  $R$  and height  $h$ , with  $h \ll R, L$ , as shown in figure 4.5.

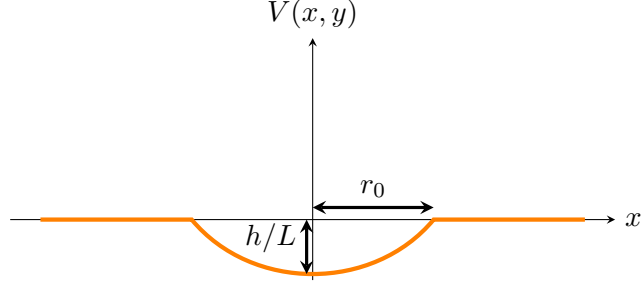


Figure 4.5: Corresponding potential of a circular dome with radius of curvature  $R$  and height  $h$ , which leads to a width of  $r_0 = \sqrt{2Rh}$ .

Using a second-order Taylor expansion around  $x, y = 0, 0$ , the corresponding height profile is

$$m_1(x, y) = 0 \quad (4.46)$$

$$m_2(x, y) \approx \begin{cases} h \left(1 - \frac{x^2+y^2}{2Rh}\right) & x^2 + y^2 \leq 2Rh = r_0^2 \\ 0 & \text{else} \end{cases} \quad (4.47)$$

$$n(x, y) \approx \begin{cases} 1 + \frac{h}{L} \left(1 - \frac{x^2+y^2}{r_0^2}\right) & x^2 + y^2 \leq r_0^2 \\ 1 & \text{else} \end{cases} \quad (4.48)$$

$$V(x, y) \approx \begin{cases} \frac{h}{L} \left(\frac{x^2+y^2}{r_0^2} - 1\right) & x^2 + y^2 < r_0^2 \\ 0 & \text{else} \end{cases} \quad (4.49)$$

As a sanity check, we are working with sapphire samples of thickness  $L \approx 420 \mu\text{m}$ . Most domes have a height  $h \approx 2 \mu\text{m}$  and radius of curvature  $R \approx 10000 \mu\text{m}$ . Hence,  $h \ll L, R$ .

The striking feature from the previous derivation is the mathematical equivalence (at least under the approximations) of sound modes in an acoustic resonator and the "clipped" two dimensional quantum harmonic oscillator with spring constant

$$k = \frac{2h}{Lr_0^2} \quad (4.50)$$

The problem is completely separable in  $x$ - and  $y$ -axes. Each dimension gives us a one-dimensional harmonic oscillator with bound states whose energies lie below zero, which we can describe by the quantum numbers  $n_x, n_y$  (and the overall excitation number  $n = n_x + n_y$ ,  $n \in \mathbb{N} \cup 0$ ). The energies are given by

$$E = \eta(n+1) \quad \eta = \sqrt{\frac{k}{m^*}} = \sqrt{\frac{2hv_t^2}{Lr_0^2 q^2 v_{l,0}^2}} \approx \sqrt{\frac{v_t^2}{RL\omega^2}} \quad (4.51)$$

each with a degeneracy of

$$\mathcal{D}(n) = n + 1. \quad (4.52)$$

The Eigenstates correspond to the Hermite-Gaussian modes [30] of an acoustic beam; both spatial amplitudes are modulated by Hermite polynomials. The quantum harmonic oscillator is clipped, i.e. we have only a finite number of bound states. States above zero are unbound modes inside the crystal ("unbound" means acoustic modes inside the crystal that are not confined to the dome region). They correspond to higher-level Hermite-Gaussian modes whose spatial profiles exceed the dome's dimensions.

We can estimate the number of bound modes by looking at figure 4.5. The depth of the energy well is  $h/L$ , and we can estimate the number of total general energy levels as:

$$N(R, h) = \left\lfloor \frac{h/L}{\eta} \right\rfloor = \left\lfloor \sqrt{\frac{h^2 \omega^2 R}{v_t^2 L}} \right\rfloor \quad (4.53)$$

Accounting for a degeneracy  $D(n)$  for the  $n$ -th energy level (see equation 4.52), we get a total of

$$N_{total}(R, h) = \sum_{i=0}^{N(R, h)} (i + 1) = \frac{(N(R, h) + 1)(N(R, h) + 2)}{2} \quad (4.54)$$

different Eigenstates.

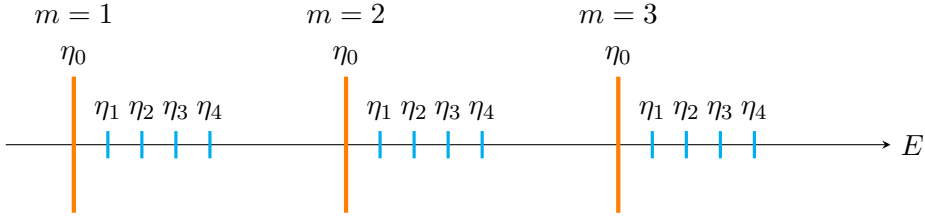


Figure 4.6: Energy spectrum of a resonator. The orange lines correspond to the Gaussian modes of a particular longitudinal resonance (labelled by the index  $m$  and  $\eta_0$ ) and cyan lines are the subsequent higher order Laguerre-Gaussian or Hermite Gaussian modes (labelled by  $\eta_i$ ).

For our values of interest ( $\omega = 2\pi \cdot 6$  GHz,  $L = 420$  μm-thick Sapphire samples), small domes ( $R = 1000$  μm,  $h = 0.4$  μm) have  $N = 2$  energy levels with  $N_{total} = 6$  different Eigenstates, but bigger domes ( $R = 5000$  μm,  $h = 4$  μm) have  $N = 56$  energy levels, with  $N_{total} = 1653$  Eigenstates! The overall spectrum of an acoustic resonator is finally clear:

- The major index  $m$  gives us the longitudinal resonances. These are equidistant over the spectrum and usually possess a Gaussian amplitude profile. They correspond to the orange lines in figure 4.6.
- The minor index  $\eta_i$  (in the circular dome case,  $i = n_x + n_y$ ) gives us the higher-order Hermite-Gaussian modes (cyan lines in figure 4.6). The number of bound modes grows both with increasing radius of curvature  $R$ , height of dome  $h$ , and frequency of the fast oscillating component  $\omega$ . In addition, it is important to notice that the energy of the complete Eigenstate is actually not  $\eta$ , but according to equation 4.45

$$E \approx \hbar\omega(1 + \eta). \quad (4.55)$$

Furthermore, this approach is only valid if  $\omega$  is a longitudinal resonance frequency of the resonator, i.e. it is a multiple integer of the FSR.

We will later see depending on the simulation's symmetry, we get either Laguerre- or Hermite-Gaussian modes; this is not surprising, as one can shift from one set to the other by simple linear combinations.

#### 4.2.1 Implementation and performance analysis

We implement the spatial meshing as a two-dimensional  $n \times n$  matrix. The potential term is a simple function evaluated at the points of interest. In order to implement the Laplacian operator, we reshape the spatial profile as a  $n^2$  single column vector and implement the standard two-dimensional Laplacian stencil

$$\nabla^2 f(x_i, y_i) = \frac{f(x_{i+1}, y_i) + f(x_{i-1}, y_i) + f(x_i, y_{i+1}) + f(x_i, y_{i-1}) - 4f(x_i, y_i)}{h^2} \quad (4.56)$$

as a  $n^2 \times n^2$  sparse matrix, where  $h = x_{i+1} - x_i = y_{i+1} - y_i$ . By neglecting the edge terms (i.e.  $i \geq n$  or  $i < 0$ ) we are assuming Neumann Boundary Conditions, and we keep the matrix Hermitian. We compared two libraries for the Eigendecomposition: ARPACK [39] (the version used by SciPy) and Spectra [40], in both cases using the Shift-and-Invert Method for Eigendecompositions, ideal for determining the smallest eigenvalues of a matrix when they are coincidentally close to zero. For a  $n^2 \times n^2$  sparse matrix, the cost of eigenvalue decomposition is  $\mathcal{O}(n^4)$ .

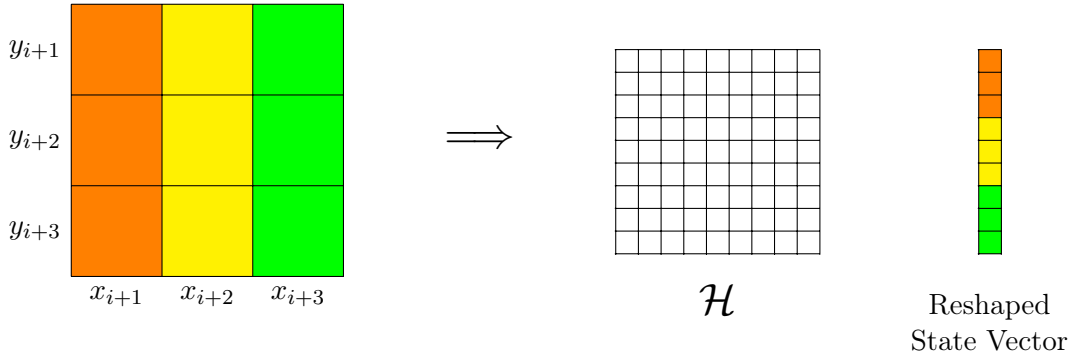


Figure 4.7: Implementation of the OSE Simulation. The two dimensional grid is reshaped as a state vector. The Hamiltonian  $\mathcal{H}$  is implemented as a  $n^2 \times n^2$  sparse matrix. The potential term corresponds to diagonal entries and the kinetic term is implemented using the standard two-dimensional Laplacian stencil.

Unfortunately the algorithm is iterative and hence, non parallelizable. The only available performance gain comes from parallelized matrix multiplications. This can be achieved with architecture-specific BLAS Libraries (Basic Linear Algebra Subroutines), which are often optimized for a single architecture. Furthermore, coarse meshings ( $n < 160$ ) lifts the degeneracies for higher energy levels, which is inaccurate from the theoretical point of view. For the examples below, we are using a mesh of  $160 \times 160$  points, which usually takes 45 minutes on the EULER Scientific Computing Cluster, with a memory footprint in the single GB range.

### 4.3 Simulation results

We will firstly look at circular domes characterized by their radius of curvature  $R$  and height  $h$ . They are essentially described by the following height profile

$$h_{cir}(x, y) = \begin{cases} h - R + \sqrt{R^2 - x^2 - y^2} & x^2 + y^2 \leq 2Rh - h^2 \\ 0 & \text{else} \end{cases} \quad (4.57)$$

According to equations 4.51 and 4.53, changing the parameters  $R$  and  $h$  should yield corresponding changes in the spectrum. Increasing the dome height corresponds to an increase in the potential well, effectively displacing the states further below in the energy axis. Increasing the radius of curvature corresponds to a reduction of the spring constant, which makes the potential flatter; the spacing between energy levels is reduced, as a function of  $R^{-1/2}$ . The Eigenstates, on the other hand, should remain unchanged up to scaling factors, as the parametric changes only modify the spring constant and the energy offset while still retaining mathematical equivalence to the quantum harmonic oscillator.

#### 4.3.1 Optical Schrödinger Equation

We will firstly consider sapphire HBAR in a plano-convex architecture of length  $L = 420 \mu\text{m}$ , with a circular dome of radius  $R = 9 \text{ mm}$  and height  $h = 0.45 \mu\text{m}$ , driven at 6 GHz (which has a manageable number of energy levels and bound states). The lowest Eigenenergies are calculated from the Hamiltonian are shown in figure 4.8. States whose energies lie above zero are unbound modes. As one can see, the degeneracies match the expected values. The spatial profiles of the nine lowest Eigenstates can also be seen in figure 4.9. Due to equation 4.55, all modes here have a frequency offset of 6 GHz, e.g. a mode labelled as  $-5 \text{ MHz}$  actually has the frequency (6 GHz - 5 MHz). For the bound part of the spectrum, we get an average energy level spacing  $\omega\eta \approx 0.746 \text{ MHz}$ .

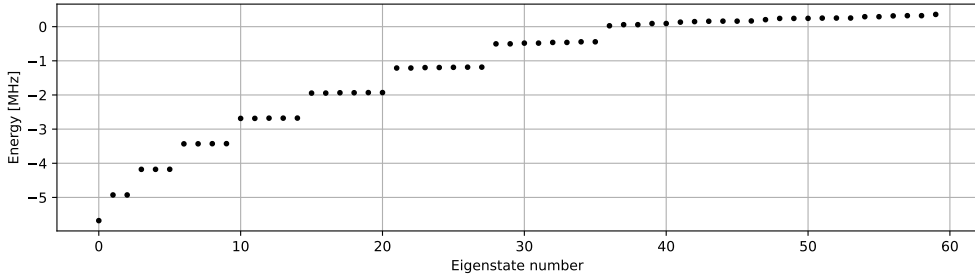


Figure 4.8: Spectra of the eigenvalues obtained in an Optical Schrödinger Equation simulator of a circular Sapphire HBAR with a circular dome of radius  $R = 9 \text{ mm}$  and height  $h = 0.45 \mu\text{m}$ , driven at 6 GHz. States whose energies lie above zero are unbound modes that are still Eigenstates of the simulational problem. Due to equation 4.55, all modes here have a frequency offset of 6 GHz, e.g. a mode at level  $-5 \text{ MHz}$  actually has the frequency (6 GHz - 5 MHz). For the bound part of the spectrum, we get an average energy level spacing  $\omega\eta \approx 0.746 \text{ MHz}$ .

A quick note regarding the Eigenstates: both libraries used for the Eigendecomposition, ARPACK [39] and Spectra [40], rely on random vectors for initialization. Especially in degenerate cases, we can get linear combinations of the Hermite-Gaussian modes for different initial vectors, which is why the spatial profiles do not match them exactly.

We can also see how the Eigenenergies change under parametric changes ( $R$  and  $h$ ), with the results shown in figure 4.10. Increasing the radius decreases the spring constant (see equation 4.50), and here we see the expected  $\sqrt{R}^{-1}$  behaviour. Increasing the dome height increases the potential depth, which is why all Eigenstates decrease in energy with increasing height.

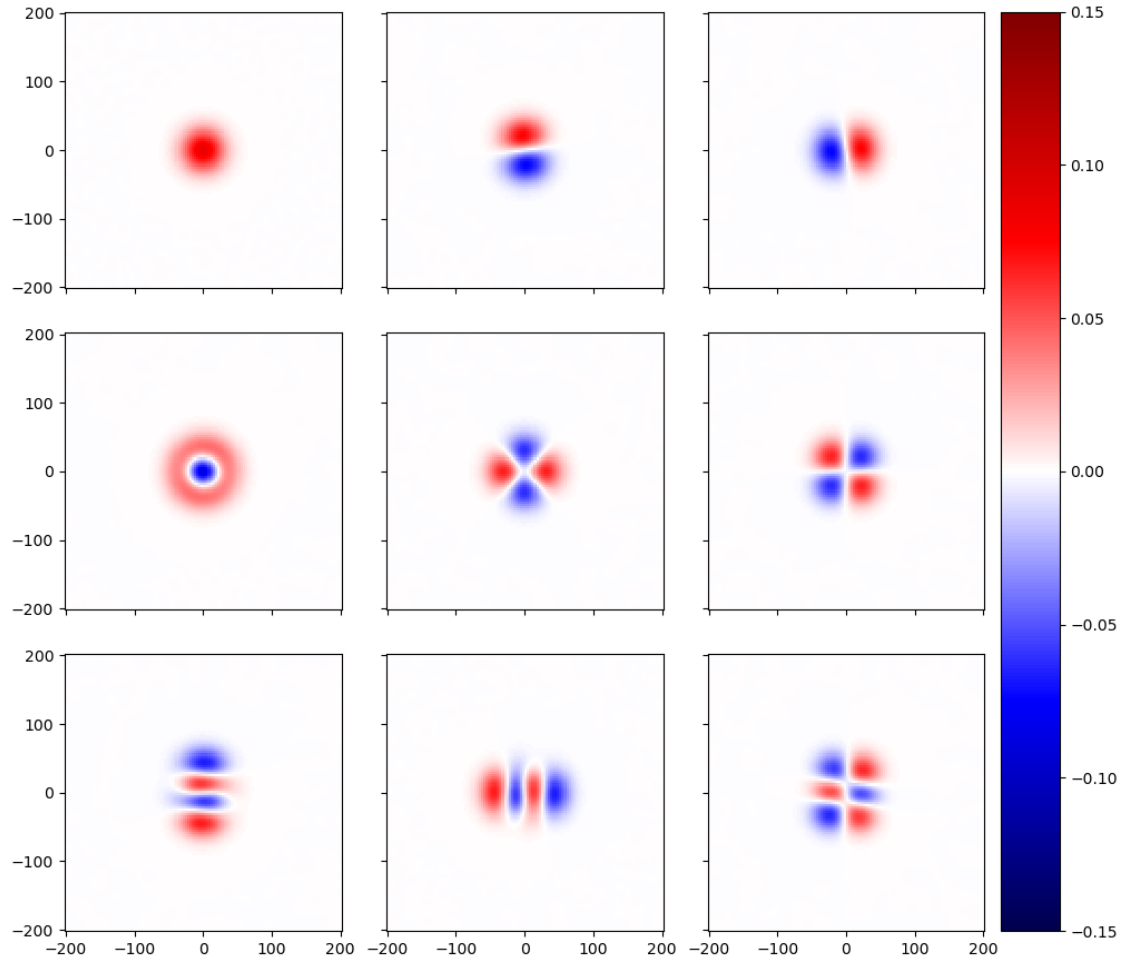


Figure 4.9: Spatial amplitude profiles of the nine lowest Eigenstates of the spectrum in figure 4.8. These profiles can be used to calculate the coupling to an external force or input via spatial integration.

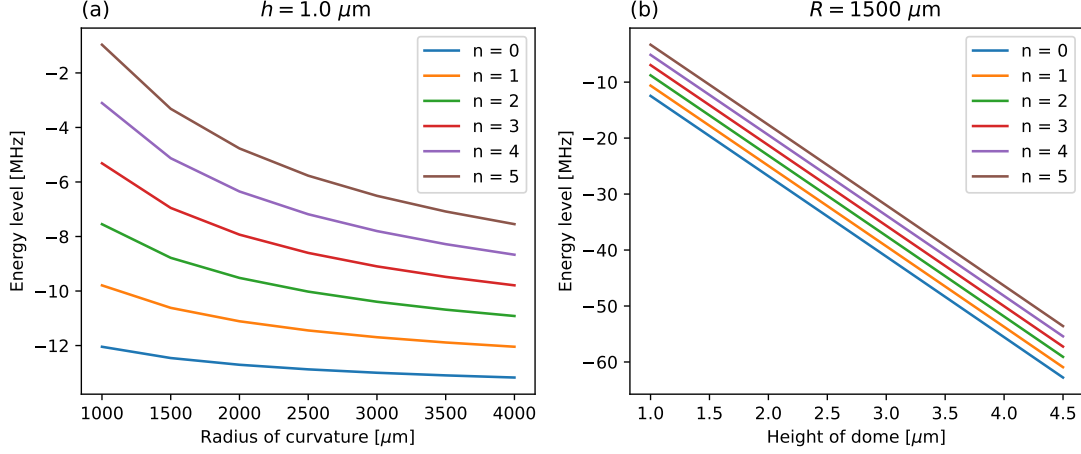


Figure 4.10: Sweeps in radius of curvature and height for a Sapphire HBAR with length  $L \approx 420 \mu\text{m}$ .

### 4.3.2 BeamProp

Considering the same HBAR from the previous section, we can perform a frequency sweep around 6 GHz. We chose a Gaussian profile for the input field (which mimics the experimental driving by a microwave antenna) with a width  $\sigma = 50 \mu\text{m}$ , as it has a non-zero spatial overlap with several different modes. The response spectrum is shown in figure 4.11, and the spatial profiles of the intensities is shown in figure 4.12.

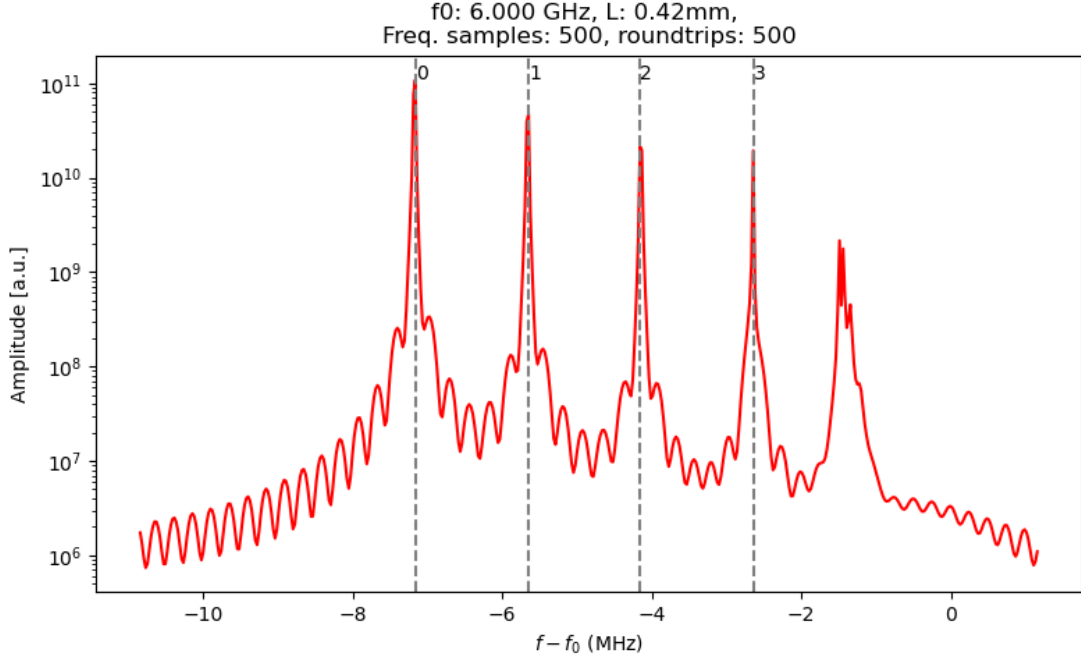


Figure 4.11: Response spectrum for a Gaussian input field of width  $\sigma = 50 \mu\text{m}$ . The vertical dashed lines show the peaks identified by our simulator.

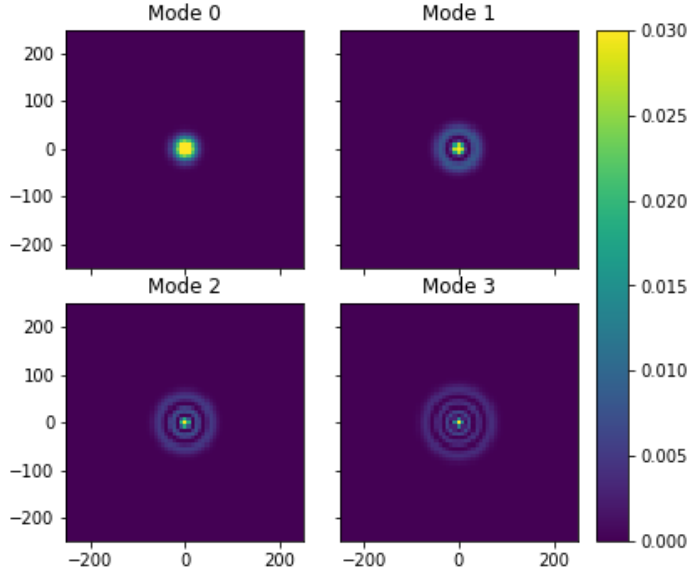


Figure 4.12: Intensity profile (i.e. absolute amplitude squared) of the modes of identified in the spectrum shown in figure 4.11.

However, after examination of the mode profiles, we notice that we couple only to the symmetric modes, which illustrates one of the main caveats of BeamProp, namely the strong dependence on the input field. We can circumvent the issue by choosing a non-centered gaussian (which would correspond to a misaligned antenna) or a half disk profile; figure 4.13 shows the spectral response for the latter forcing function, with the corresponding mode profiles shown in figure 4.14. We can outline two important results:

- The mode frequency does not depend on the input profile (as long as the spatial overlap is not zero).
- The energy level spacing for the non-symmetric forcing function  $\omega\eta \approx 0.749$  MHz, in agreement to the OSE simulations.

Furthermore, we notice a constant frequency shift for all modes compared to the OSE Simulations; this is mainly due to the fact that 6 GHz is **not** an integer multiple of the FSR (the closest resonances lie at 5.992 GHz and 6.005 GHz). For practical purposes, this mismatch does not play a significant role, as the qubits' frequencies are tunable.

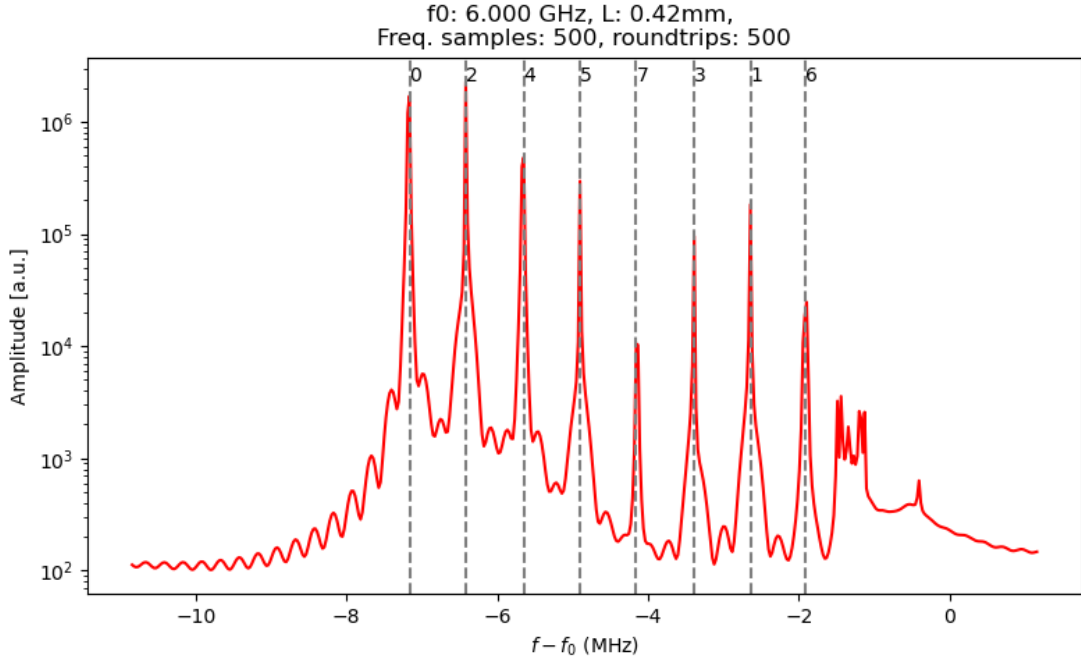


Figure 4.13: Response spectrum for a half-disk input field. We get an average energy level spacing  $\omega\eta \approx 0.749$  MHz. The vertical dashed lines show the peaks identified by our simulator, sorted by peak prominence. The extra peaks between -2 MHz and 0 MHz correspond to unbound modes.

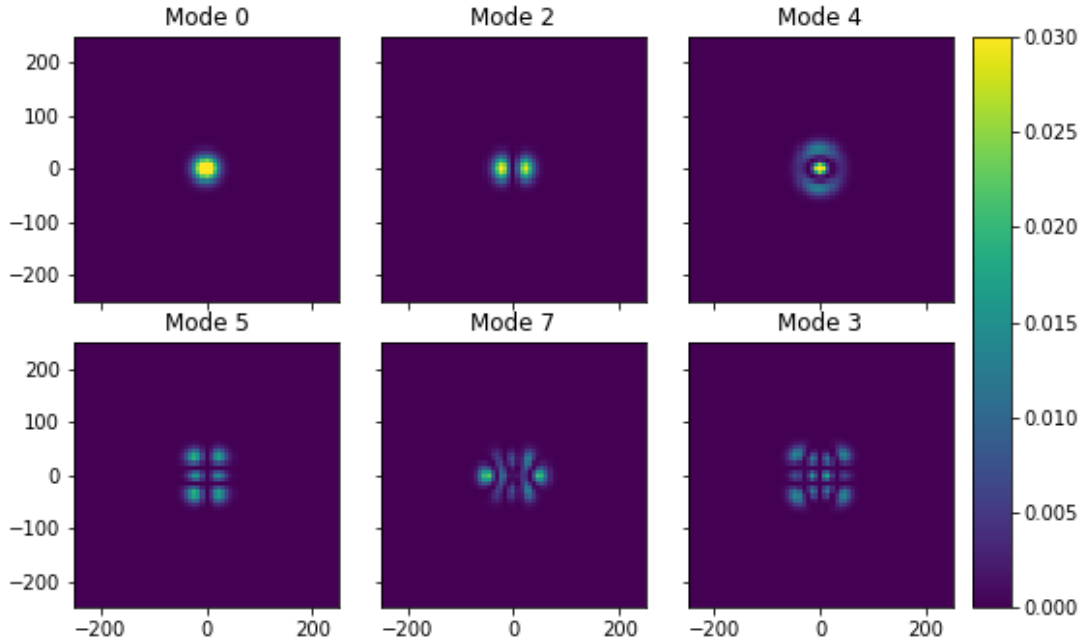


Figure 4.14: Intensity profile (i.e. absolute amplitude squared) of selected modes of identified in the spectrum shown in figure 4.13.

Whereas spatial overlap can become a limiting factor for the discovery of modes, it can also be an useful tool for achieving coupling selectivity. If we had chosen a Gaussian field whose width matches the lowest Eigenstate for the input, the spectrum would only have one peak, as shown in figure 4.15.

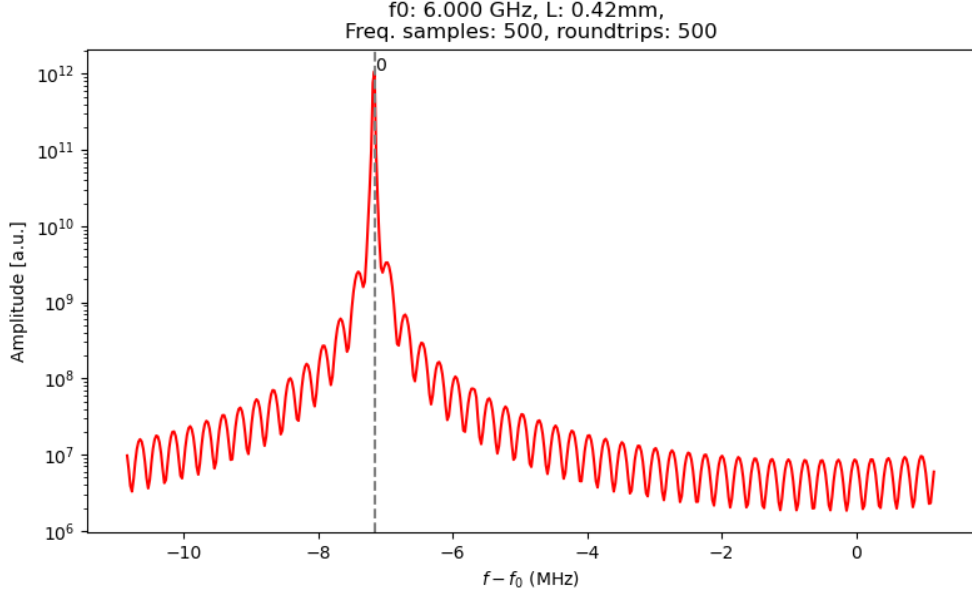


Figure 4.15: Response spectrum for an input field matching the  $n = 0$  mode spatial profile.

## 4.4 Anharmonic dome shapes

Translating the paraxial propagation of sound into an equivalent Schrödinger Equation opens up the door for a mighty tool from quantum mechanics: perturbation theory! We can essentially estimate the changes in the spectrum just by calculating the corresponding matrix elements (which are spatial integrals).

### 4.4.1 Perturbation theory

We will restrict ourselves to domes with axial symmetry and only look at perturbations of the form

$$\mathcal{H}_{x,y}^1 \propto (x^2 + y^2)^2 \quad (4.58)$$

We can restrict our analysis to the  $x$ -axis sub-problem

$$\mathcal{H}_1 \propto x_0^4 (\hat{a} + \hat{a}^\dagger)^4 \quad (4.59)$$

for some intuition. The factor  $x_0 = (\sqrt{2m*\eta})^{-1}$  is the zero-point motion,  $\hat{a}$  and  $\hat{a}^\dagger$  are the corresponding ladder operators. From perturbation theory [41], we know that the matrix elements are

$$M_{m,n} = \langle m | x_0^4 (\hat{a} + \hat{a}^\dagger)^4 | n \rangle. \quad (4.60)$$

with the corresponding first-order energy shifts  $\Delta E_{1,n}$

$$\Delta E_{1,n} = M_{n,n} \quad (4.61)$$

Instead of calculating all coefficients explicitly, we can opt for a more intuitive argument that will help us understand why both shifts in this particular case will be positive. Each time the operator  $(\hat{a} + \hat{a}^\dagger)$  is applied, the state  $|n\rangle$  is mapped to a superposition of  $|n+1\rangle$  and  $|n-1\rangle$ . Further applications yield further states, which in the end range from  $|n+4\rangle$  to  $|n-4\rangle$ , as seen in figure 4.16.

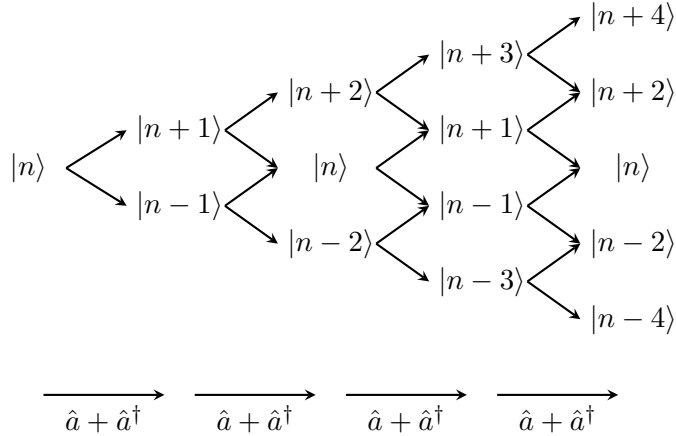


Figure 4.16: Tree of states spanned by the repeated application of the normalized position operator  $(\hat{a} + \hat{a}^\dagger)$ .

It is important to notice two important aspects:

1. For a state  $|n\rangle$ , the raising operator yields a factor of  $\sqrt{n+1}$  and the lowering operator yields a factor of  $\sqrt{n-1}$ . Overall, a bigger proportion is mapped to higher energy states than to lower ones, and always with positive factors.
2. For low energy states  $n \leq 3$ , the lower parts of the tree do not exist, as annihilation of the vacuum state  $|0\rangle$  yields no state at all.

As all prefactors are positive numbers, the first-order energy shifts are positive for positive anharmonicities. The shifts are more pronounced for higher level states, which results in spread of the spectrum. On the other hand, for negative fourth order coefficients, both shifts are negative, but still of higher magnitude for higher level states. These characteristics result in the concentration of the spectrum. Previous work [42] has shown that Gaussian and Cosine shapes of a dome, both with a negative fourth order coefficient in their Taylor expansions, yield a negative anharmonicity, with the difference of the energy levels decreasing for higher level modes.

We are interested in seeing the spectral changes of a dome with respect to the fourth order term. We will define our height profile as

$$h_{anh}(x, y, h, R, a) = -a \cdot (x^2 + y^2)^2 + b \cdot (x^2 + y^2) + c \quad (4.62)$$

and clip all values beyond the first zero crossing, as seen in figure 4.17. This height profile has a height  $h = c$  and effective radius of curvature  $R = -1/2b$  at the point  $(x, y) = (0, 0)$ .

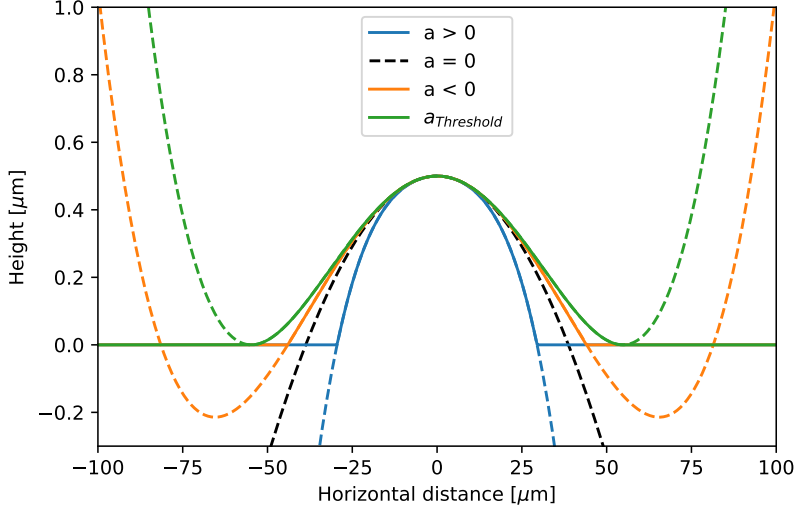


Figure 4.17: Anharmonic dome profiles. For the concerned profiles, we simply assume the profile to be zero after the first zero crossing, ignoring the further revivals (dashed lines). The green line corresponds to the minimal anharmonic profile that still crosses the  $x$ -axis, which corresponds to the condition  $b^2 \geq -4ac$ .

As we saw on the earlier section (and keeping in mind that the quadratic term  $b$  is negative), decreasing the anharmonicity term  $a$  yields a more compressed spectrum (smaller spacings between the energy levels). Increasing the anharmonicity, on the other hand, only increases the spacing. Hence we can outline two different strategies:

1. Decrease the anharmonicity and compress the spectrum of bound modes. This should open up a bigger energy space between the highest bound mode of a previous FSR and the lowest bound mode of the next one (in figure 4.6 they are the right-most cyan lines and the orange lines, respectively). A bigger space in the spectrum means reduced dispersive coupling to the other unwanted modes.
2. Increase the anharmonicity and spread out the spectrum. The modes are displaced further from each other; if some exceed the height of the potential well, they cannot be bounded anymore and hence disappear from the spectrum.

Before we proceed, we need to set some boundaries. If we decrease the value of  $a$  too much, we will not get any zero crossings; to avoid this, we solve for the zeros of the previous equation and find the following condition

$$b^2 \geq -4ac \iff -\frac{1}{16R^2h} \leq a. \quad (4.63)$$

Another thing we must consider is the sample free spectral range; as we change the shape of the surface, all sets of cyan lines in figure 4.6 will suffer a similar energy change; if one of these lines crosses an orange line, we can have modes of different longitudinal resonances interfering with each other. To avoid such a situation, we can limit the height of our domes such that the potential depth in frequency does not exceed one FSR. Making use of equation 4.45, and reminding ourselves that the potential well has a depth of  $\omega h/L$ , we find that a Sapphire HBAR with an  $FSR \approx 13.3$  MHz has a height limit of  $h_{max} \approx 0.93 \mu m$ .

#### 4.4.2 OSE Simulations

For the case of a dome of height  $h = 0.9 \mu\text{m}$  and effective radius of curvature  $R = 1500 \mu\text{m}$ , we can plot the evolution of the energy levels as a function of the anharmonic term, as shown in figure 4.18. As soon as the energy level rises above zero, we stop considering it.

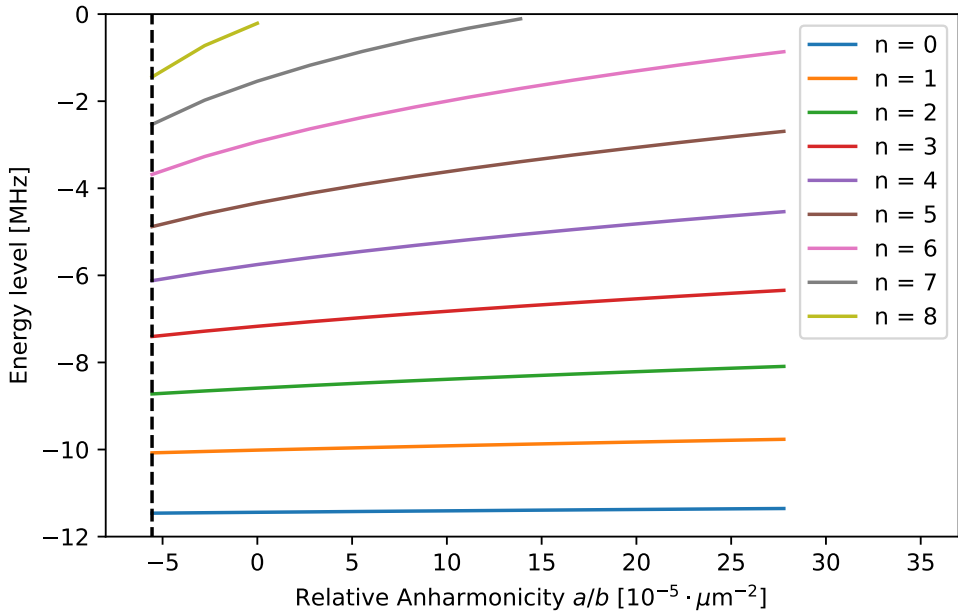


Figure 4.18: Anharmonic dome spectrum evolution a dome of height  $h = 0.9 \mu\text{m}$  and effective radius  $R = 2500 \mu\text{m}$  as a function of the relative anharmonicity  $a/b$ . The black vertical dashed line indicates the minimal anharmonicity satisfying the condition  $b^2 \geq -4ac$ .

For better visualization, we define the **mode anharmonicity** [42]:

$$\alpha_i = \frac{(f_{i+1} - f_i) - (f_1 - f_0)}{(f_1 - f_0)} \quad (4.64)$$

where  $f_i$  is the energy level for the  $i$ -th mode. In a harmonic oscillator, all modes have the same frequency spacing, hence  $\alpha_i = 0$  for all modes of interest. For the two aforementioned strategies, we see different outcomes:

1. Decreasing the anharmonicity slightly compresses the spectrum. Nevertheless, it yields a unwanted side effect: the anharmonic term decreases the energy of previously unbounded modes to the bounded part of the spectrum. We cannot expect a mode free region in the spectrum between FSR groups.
2. Increasing the anharmonicity slightly spreads out the spectrum. Choosing appropriate parameters, such as in figure 4.18, a slight anharmonic perturbation makes the  $n = 7, 8$  energy levels unbounded, and frees up some space in the upper part of the spectrum.

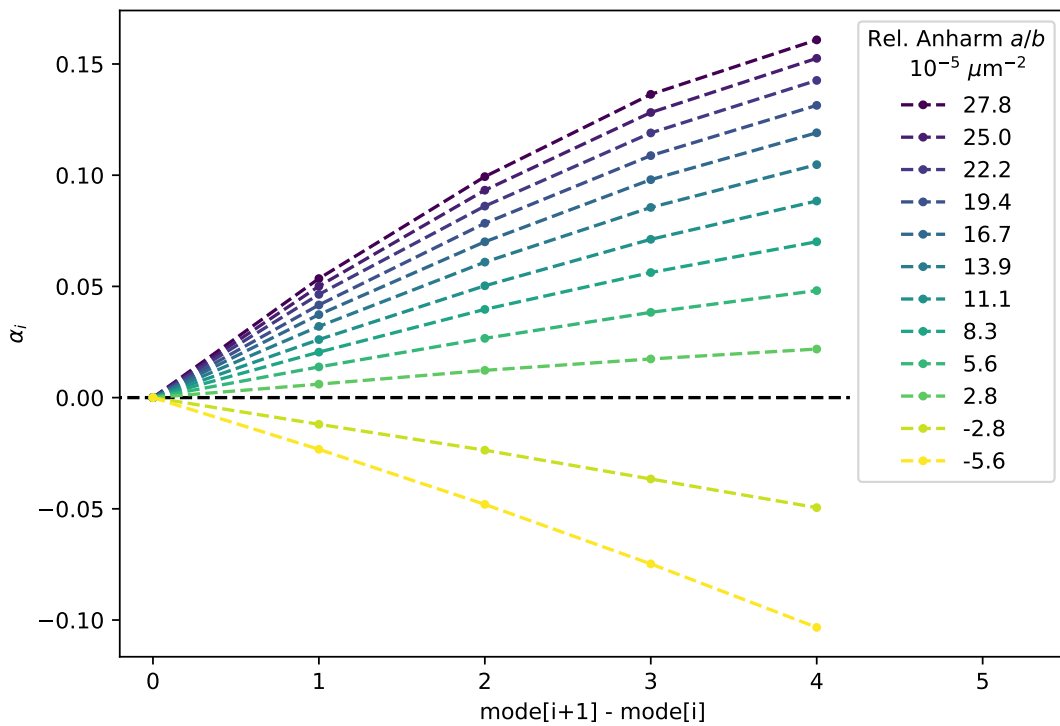


Figure 4.19: Mode anharmonicities  $\alpha_i$  for different relative dome anharmonicities  $a/b$  (in units of  $10^{-5} \mu\text{m}^{-2}$ ). The horizontal dashed line represents the case of a harmonic oscillator, where the frequency spacing remains constant.

# Chapter 5

## Fabrication tools

As seen in section 4.4, anharmonic dome shapes may exhibit unusual acoustic spectra. The logical next step is the assessment of whether the fabrication of said domes is possible, and what limitations might exist. Previous work on the design of acoustic resonators [27] employs solvent reflow for the creation of  $\mu\text{m}$ -tall circular domes with an astounding root mean square roughness on the sub-nanometer order; nevertheless, no shapes other than circular domes can be produced (see section 5.2 for a more thorough explanation). In this chapter, we will introduce two different methods for grayscale lithography and explain how they give us more freedom in the choice of dome shapes.

### 5.1 Grayscale Lithography

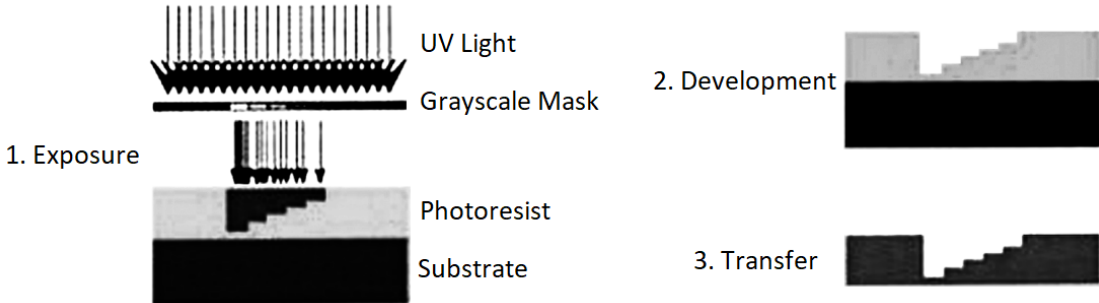


Figure 5.1: Diagram explaining masked grayscale lithography; by fabricating a mask that regulates the amount of intensity of each pixel, we can underexpose the photoresist (step 1) and hence create a (post-developed) 3D structure (step 2); the latter can be later transferred to the substrate over suitable etching techniques (step 3). Adapted from [43].

One suitable candidate for the nanofabrication of 3D patterns is grayscale UV-lithography [43]: whereas conventional lithography processes expose thin layers of photosensitive chemicals, this process consists in underexposing thicker resists. The partial exposure bleaches the top of the resist, while leaving the bottom intact. The thickness of the exposed layer increases monotonically with dose (see figure 5.1); moreover, the post-exposure development only dissolves the exposed resist, allowing one to carve three dimensional patterns in the latter. The resulting three dimensional structures can be transferred to the substrate via suitable etching techniques. Our photoresist of choice,

AZ4562 from Microchemicals GmbH<sup>©</sup>, yields a thickness of  $8.77\ \mu\text{m}$  after a 2000 rpm spin [44]. For a more detailed description of grayscale lithography including the challenges and limitations of this method, we refer to previous work [42]. We present two different methods to modulate the dose of UV-light on the substrate:

1. Laser writers with variable power (direct written grayscale lithography)
2. Grayscale masks (masked grayscale lithography)

Both methods are further explained in the following subsections.

### 5.1.1 Masked grayscale lithography

Our masked grayscale lithography is based on the principle of the effective pixel; for most thin resists in binary masked lithography, the exposed regions correspond to the openings of the mask (as shown in figure 5.2a). For thicker resists, beam dispersion is not negligible anymore; nearby points under opaque regions of the mask do get a certain level of exposure. We define the effective pixel length  $l_{EP}$  as the length of the exposed region, as shown in figure 5.2b.

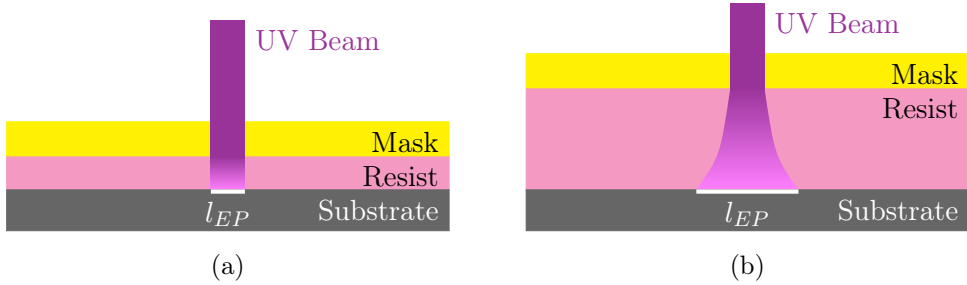


Figure 5.2: A comparison of masked exposure of (a) thin and (b) thick resist. Diffraction is negligible in thin substrates, hence the effective pixel usually matches the mask opening; in thick substrates, diffraction increases the effective pixel size. We define the effective pixel as the exposed length on the substrate. Figures adapted from [42].

From previous work [42], we know the effective pixel length  $l_{EP}$  of our photoresist (AZ4562 from Microchemicals GmbH<sup>©</sup>) is  $l_{EP} \approx 2.6\ \mu\text{m}$ . Furthermore, the effective pixel does not change significantly with aperture size in the mask, however the effective UV dose does: it is proportional to the aperture area. We can use these characteristics to conceptualize graytone pixels, which modulate intensity behind the mask. Following a similar approach to [45], we divide the dome into pixels with side length  $l_{EP}$ ; each pixel contains a square aperture of size  $l_g$  (which can vary between pixels), and hence the effective dose  $d$  under the graytone pixel is

$$d = D_0 \cdot F \quad F = \frac{l_g^2}{l_{EP}^2} \quad (5.1)$$

whereas  $D_0$  is the nominal UV dose from the mask aligner, which is easily adjustable, and  $F$  is the **filling factor** or simply the ratio between transparent and total areas of the pixel (e.g. a fully transparent pixel corresponds to  $F = 1$  and a pixel with  $F = 0.75$  has 75% of its total area transparent, and 25% opaque).

There are however, three main limiting factors arising from the mask fabrication (see figure 5.3 for a descriptive diagram):

1. **Critical dimension  $l_{CD}$** : structures with an area smaller than  $l_{CD}^2$  are not properly etched in the mask's opaque chromium layer; in essence, it defines a lower boundary for the grayscale pixels, whose square aperture dimensions must exceed  $l_{CD}$  in both  $x$ - and  $y$ -axis. For our case,  $l_{CD} \approx 1.1 \mu\text{m}$ .
2. **Addressable grid  $l_{AD}$** : the laser writing the mask cannot be displaced with arbitrarily small increments; rather, it moves in steps  $dx = dy = l_{AD}$ . In essence, it restricts the allowed graytones to a discrete scale. We define
  - Graytone 0 is an aperture of dimensions  $l_{CD} \cdot l_{CD}$
  - Graytone 1 is an aperture of dimensions  $(l_{CD} + l_{AD}) \cdot l_{CD}$
  - Graytone 2 is an aperture of dimensions  $(l_{CD} + l_{AD}) \cdot (l_{CD} + l_{AD})$
  - Graytone  $n = n_x + n_y$  is an aperture of dimensions  $(l_{CD} + n_x \cdot l_{AD}) \cdot (l_{CD} + n_y \cdot l_{AD})$ .

For our case,  $l_{AD} \approx 0.03 \mu\text{m}$ .

3. **Minimal distance  $l_{MD}$** : opaque chromium strips in the mask thinner than  $l_{MD}$  are completely removed in the etch process; in essence, it defines an upper bound for the grayscale pixels, as two neighboring high grayscale pixels need a combined opaque strip of length  $l \geq l_{MD}$ . We assumed  $l_{MD} = 0.15 \mu\text{m}$  for the calibration, but after visual inspection we recommend at least  $l_{MD} = 0.3 \mu\text{m}$  and a corresponding increase of the effective pixel to  $l_{EP} = 2.8 \mu\text{m}$ .

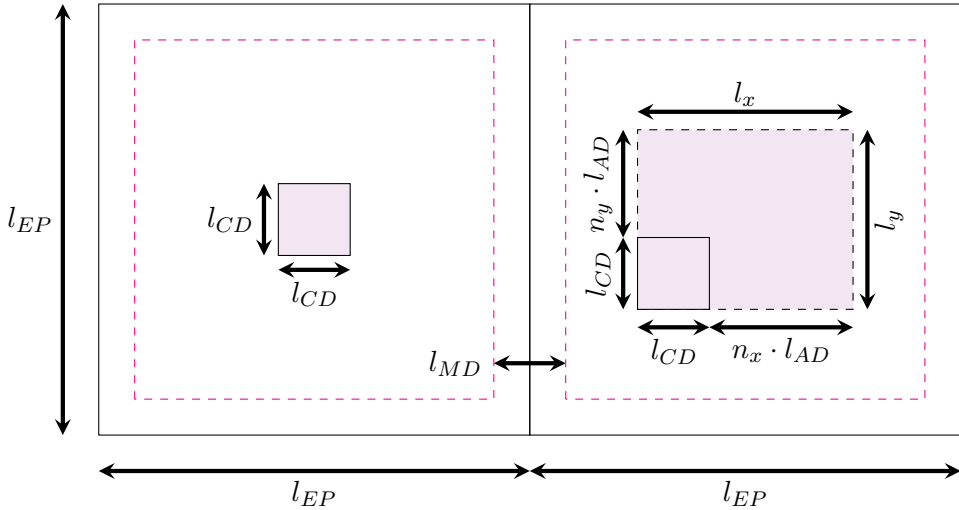


Figure 5.3: Diagram of neighboring grayscale pixels with its defining dimensions (addressable grid  $l_{AD}$ , critical dimension  $l_{CD}$ , effective pixel  $l_{EP}$  and minimal distance  $l_{MD}$ ). White and violet areas correspond to opaque and transparent regions, respectively. The magenta dashed squares are the maximal graytones under the minimal distance constraint. The left structure is a pixel corresponding to graytone  $g = 0$ , i.e. a window with dimension  $l_{CD}^2$ , whereas the right graytone corresponds to graytone  $g = n_x + n_y$ .

Taking all previous parameters into consideration, one can calculate the following quantities:

- The **number of available graytones**

$$N_{EP} = 2 \cdot \left\lfloor \frac{l_{EP} - l_{MD} - l_{CD}}{l_{AD}} \right\rfloor. \quad (5.2)$$

For our parameters, we get  $N_{EP} = 90$ , which is more than enough.

- The **filling factor** of a gray pixel  $g = n_x + n_y$

$$F(g) = \frac{l_x \cdot l_y}{l_{EP}^2} = \frac{(l_{CD} + \lfloor g/2 \rfloor \cdot l_{AD}) (l_{CD} + (\lfloor g/2 \rfloor + g \bmod 2) \cdot l_{AD})}{l_{EP}^2} \quad (5.3)$$

$$= \frac{l_{CD}^2 + (n_x + n_y) \cdot l_{AD} \cdot l_{CD} + n_x \cdot n_y \cdot l_{AD}^2}{l_{EP}^2} \quad (5.4)$$

which is just the ratio between the transparent area within a pixel and it's full area;  $g \in \mathbb{N} \cup 0$  is the graytone number.

- The (approximate) **graytone from filling factor** (i.e. the inverse of the previous function)

$$g(F) = \text{round} \left( 2 \cdot \frac{\sqrt{F \cdot l_{EP}^2 + \frac{l_{AD}^2}{8}} - l_{CD}}{l_{AD}} \right) \quad (5.5)$$

and  $\text{round}(x)$  rounds  $x$  to the nearest integer.

### 5.1.2 Direct-written laser grayscale lithography

The direct laser-written method is similar to binary laser writer, with the additional feature that the intensity of light is regulated at each pixel. Specially designed laser writers (in our case, the DWL 66+ from Heidelberg Systems<sup>©</sup>) have the ability to modulate the laser beam through the use of digital electronics and acousto-optic modulators, allowing for a total 128 possible graytones, with 0 corresponding to total darkness and 127 corresponding to maximal intensity, which is also separately adjustable.

### 5.1.3 From graytones to height profiles

We need to determine how much exposure corresponds to each height. In the case of masked lithography, although the beam diffraction is assumed to be contained within  $l_{EP}$  (as shown in figure 5.2b), we do notice some edge effects when different graytone pixels are paired together. In order to get an "unbiased" calibration, we designed a calibration array (as shown in figure 5.4). Each array object is a 100  $\mu\text{m}$  long square grid of identical graytone pixels. Along the array's rows we increase the transparent window area (consequently increasing the filling factor  $F$ , graytone number  $g$  and the effective dose  $d$ ); along the columns we increase the effective pixel size. The average height at the center of the calibration square is then interpreted as the resist height of the corresponding graytone.

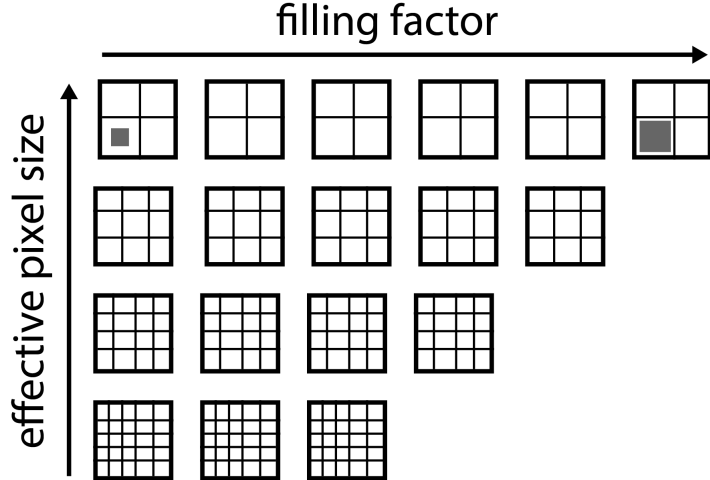


Figure 5.4: Calibration array with varying  $l_{EP}$  along the columns and the window sizes (and consequently filling factor  $F$ , graytone number  $g$ , and effective dose  $d$ ) along the rows. Each array object is actually a grid of several graytone pixels of the same parameters for an undisturbed calibration [42].

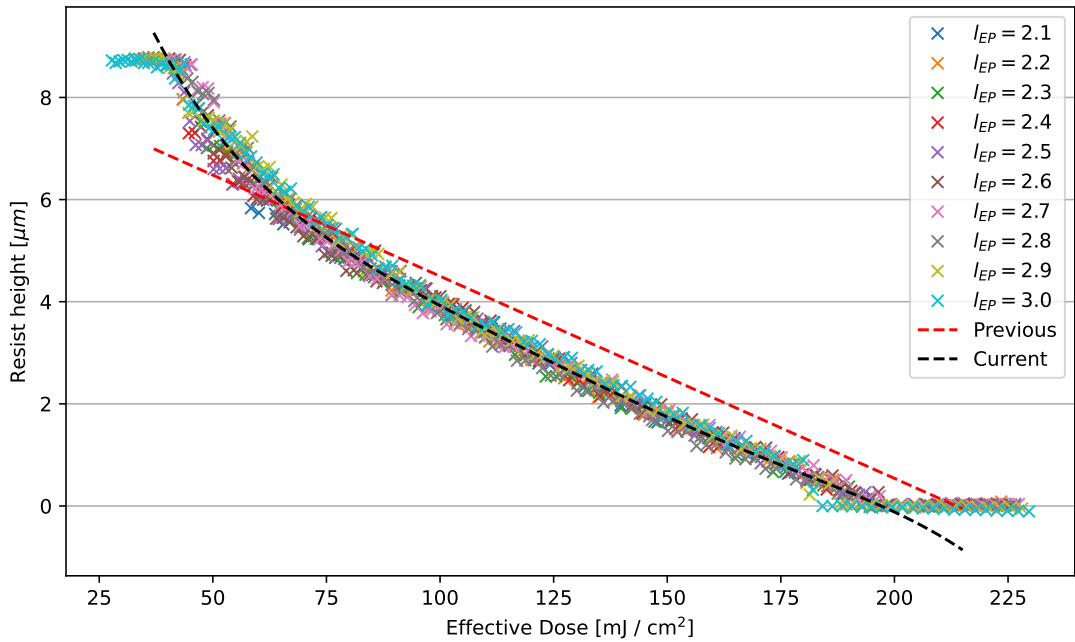


Figure 5.5: Exposure curve of AZ4562 in the EVG 620NT Mask Aligner by EV Group<sup>©</sup> for graytones based on different effective pixels, assuming an initial resist thickness of 8.77  $\mu\text{m}$  [44]. All curves are generated on the same exposure with nominal dose  $D_0 = 250 \text{ mJ cm}^{-2}$ ; different effective doses are obtained by varying the filling factor, as shown in figure 5.4. The red dashed line corresponds to the calibration curve from previous work [42], which was used as a reference; the black dashed line corresponds to equation 5.6.

Calibrations of the resist in sapphire samples with our mask aligner yield the exposure curve (black dashed line) shown in figure 5.5. All curves are generated on the same exposure with nominal dose  $D_0 = 250 \text{ mJ cm}^{-2}$ . The relation is monotonic (i.e. higher dose corresponds to less resist left) yet not linear; least squares regression yields

$$\begin{aligned} h_{EVG}(d) = & 20.85 - 0.5049 \cdot d + 6.796 \cdot 10^{-3} \cdot d^2 - 5.010 \cdot 10^{-5} \cdot d^3 + 1.834 \cdot 10^{-7} \cdot d^4 \\ & - 2.641 \cdot 10^{-10} \cdot d^5 \end{aligned} \quad (5.6)$$

where  $d$  is the effective dose and  $h_P^{EVG}$  is the height left of resist.

Masked grayscale lithography has one main advantage over direct laser written: it has a quick exposure time ( $\sim 100$  seconds), independent of the number of structures generated, completely suitable for mass production. Its main limiting aspect is the quality of the mask; for small graytones the fabricated structures exhibit a high degree of accuracy (see fig. 5.6a); for neighboring pixels of higher graytones, the thin chromium strips are sometimes completely removed at the etch process (see fig. 5.6b). Given that the regions of higher graytones correspond to the edge of the dome, and that most of the acoustic power is concentrated in its center, these defects should not play a significant role.

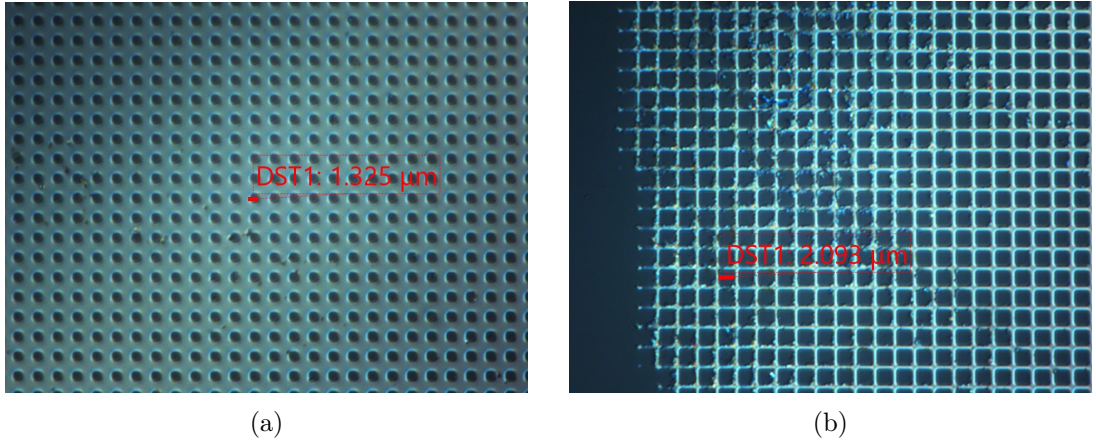


Figure 5.6: Grayscale mask under optical microscope on top illumination setting (dark regions are transparent, bright regions are opaque). The regions containing (a) low-graytone pixels are faithfully reproduced, whereas regions with (b) high-graytone pixels have some opaque strips removed in the fabrication process. These masks were generated assuming a minimal distance  $l_{MD} = 0.15 \mu\text{m}$ , but a value of  $l_{MD} = 0.3 \mu\text{m}$  seems more appropriate.

Calibrations of the resist in sapphire samples with our direct laser writer yield the exposure curve shown in figure 5.7. The relation is monotonic (i.e. higher dose corresponds to less resist left) yet not linear; least-squares regression yields

$$h_{DWL}(P) = 15.45 - 1.303 \cdot P + 0.04280 \cdot P^2 - 5.628 \cdot 10^{-4} \cdot P^3 \quad (5.7)$$

where  $P$  is the laser power in mW and  $h_P^{DWL}$  is the height left of resist. The calibration did not explicitly use the grayscale setting; we are assuming a linear relation between the graytone number and resulting laser power from the machine.

Laser written samples have an increased degree of accuracy compared to its counterparts which undergo masked grayscale lithography, primarily because it is not subject to

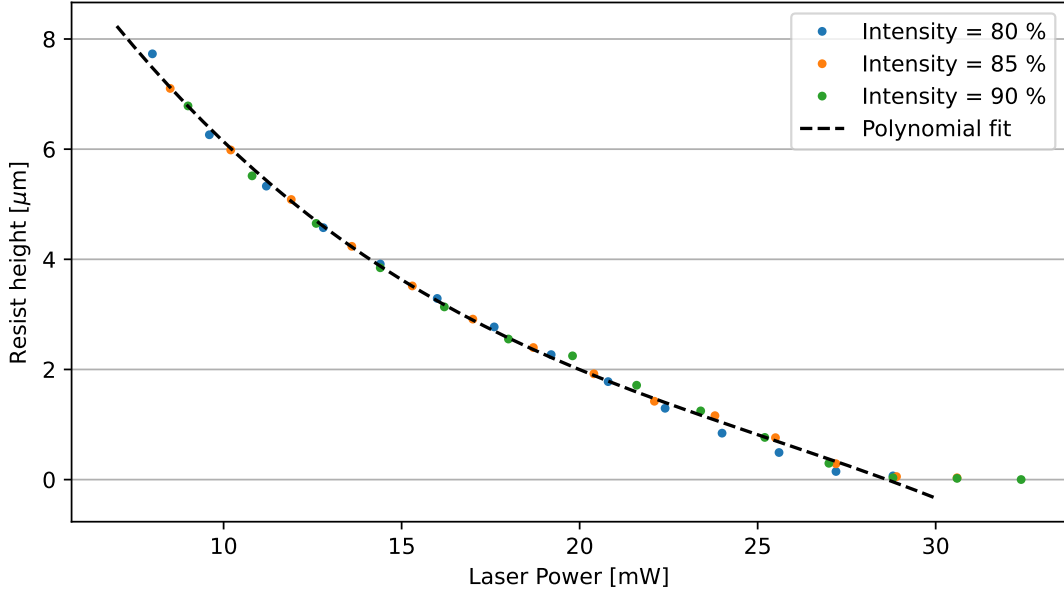


Figure 5.7: Exposure curve of AZ4562 in the Laser Writer DWL 66+ by Heidelberg Systems<sup>©</sup> (n-over-4 mode, focal offset = +60%) with the third-order best-fit polynomial. The different colors represent different intensity settings, and the laser power in the horizontal axis corresponds to the laser power shown in the DWL 66+ multiplied by the intensity setting. We are assuming an initial resist thickness of 8.77  $\mu\text{m}$  [44]. The calibration did not explicitly use the grayscale setting; we are assuming a linear relation between the graytone number and resulting laser power from the machine.

mask fabrication defects. Its main limitation is the writing time: the latter can exceed one hour for a batch of 30 domes in a sample. It also increases linearly with the number of domes, whereas masked grayscale lithography has a constant exposure time.

#### 5.1.4 From height profiles to graytones

Given the monotone exposure curves in thick photoresists, as seen in figures 5.5 and 5.7, we need a method for translating an arbitrary two dimensional height profile into a spatially varying intensity profile. The main idea is to find the inverse of equations 5.6 and 5.7 through regression:

$$d_{EVG}(h) = 196.0 - 26.32 \cdot h + 0.04294 \cdot h^2 + 0.05096 \cdot h^3 + 0.01935 \cdot h^4 - 0.001449 \cdot h^5 \quad (5.8)$$

$$P_{DWL}(h) = 28.66 - 4.978 \cdot h + 0.375 \cdot h^2 - 0.01014 \cdot h^3 \quad (5.9)$$

Following the approach [45], we divide the height profile into several pixels of length  $l_{EP}$ , each containing the average height inside the region. The previous equations convert this array of height pixels into an array of required intensities. The procedure varies depending on the chosen method:

- **Masked lithography:** assuming the effective pixel to be constant throughout the graytone scale, we convert each intensity into a integer graytone number  $g$  using

equation 5.5. The dimensions of the grayscale window ( $l_x, l_y$ ) shown in figure 5.3 are easily obtained by modular arithmetic:

$$n_x = \lfloor g/2 \rfloor \quad n_y = \lfloor g/2 \rfloor + g \bmod 2 \quad (5.10)$$

$$l_x = l_{EP} + n_x \cdot l_{AD} \quad l_y = l_{EP} + n_y \cdot l_{AD} \quad (5.11)$$

Hence we can translate a two-dimensional height profile into a pattern of grayscale pixels (in a .svg or .gds file format) that can be used by mask manufacturers.

- **Direct laser-written lithography:** each intensity pixel is encoded into a grayscale bitmap image, which is the preferred file format by the laser writer.

## 5.2 Solvent reflow

After the development process, some domes may exhibit a high degree of roughness on the surface. Based on previous work [27], we can reduce the roughness by solvent reflow. The process is shown in figure 5.8 and is fairly simple: after the exposure, the resist is soft-baked at a temperature lower than the glass temperature. The dome is in a meta-stable state: solid enough to preserve its structure, yet susceptible to shape changes under certain conditions.

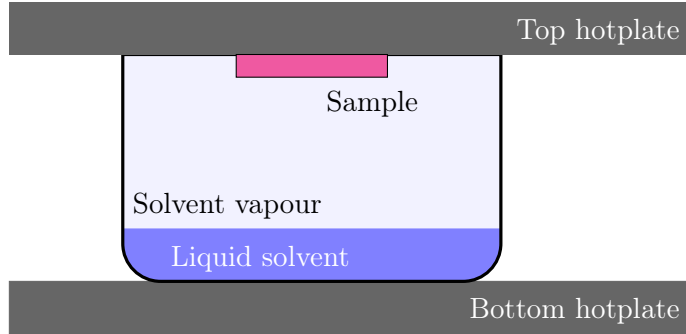


Figure 5.8: Solvent reflow of a sample.

By placing the sample inside a chamber with evaporated solvent, the dome can change its shape. From a thermodynamic perspective, the dome behaves as a liquid droplet; its Gibbs free energy  $G$  depends on the surface tension  $\sigma$

$$G = G_0(p, T, V) + \int_{\partial D} \sigma d\vec{A} \quad (5.12)$$

where  $G_0(p, T, V)$  corresponds to all other thermodynamic potentials, and the integral is performed over the dome surface. From an analytical standpoint, we know that droplets arrange themselves to minimize the surface tension along the object. To a good approximation, one can treat the surface tension as constant along the surface. Rough surfaces have a bigger surface area than smooth surfaces, and the shape with a minimal surface area under the constraint of a constant volume is the sphere sector. We can conclude that short periods of solvent reflow reduce the roughness of the domes; longer periods converts them into spherical domes. Optimizing the reflow time between 240 and 300 seconds yields smooth surfaces with non-circular shapes (see section 6.1.4).

# Chapter 6

## Sample measurements

In the previous chapter we confirmed the suitability of thick photoresists for grayscale lithography; moreover, we were able to calculate functions that translate height profiles into intensity profiles that can be used in masked or direct laser grayscale lithographies, effectively allowing us to write the sought anharmonic domes. In this section, we will analyze and quantify the quality of the written structures.

### 6.1 Masked grayscale lithography

#### 6.1.1 Calibration arrays

The graytone grids are measured in one long profilometer sweep. The initial spectrum exhibits a high degree of roughness with some overall curvature along the wafer, which may be attributed to resist variations. (see figure 6.1a); a simple gaussian filter and least squares regression on the top yields a more useful curve that can be easily analyzed using peak finding algorithms, as shown in figure 6.1b. We then determine the height difference between surface and graytone, we determine the height as the initial thickness (which we assume to be  $8.77 \mu\text{m}$  [44]) minus the height difference. Combining all points and assigning the corresponding dose based on equation 5.1, we can obtain the calibration profile shown in figure 5.5.

#### 6.1.2 Domes

Domes produced by masks do not exhibit the quality of their laser-written counterparts; nevertheless, the shorter fabrication process enabled a mass production of domes of different shapes and sizes, which was useful to optimize other fabrication parameters, such as the time spent under solvent reflow. In order to test the limits of grayscale lithography, we designed a mask with more than 50 domes. We tried every combination of the following parameters:

- **Shapes:** Circular, Cosine and Gaussian.
- **Apex heights:** 4.0, 5.0, 6.0, and  $6.4 \mu\text{m}$ .
- **Radii of curvature:** 1250, 1750, 2500, 3750, 5000, and 10000  $\mu\text{m}$ .

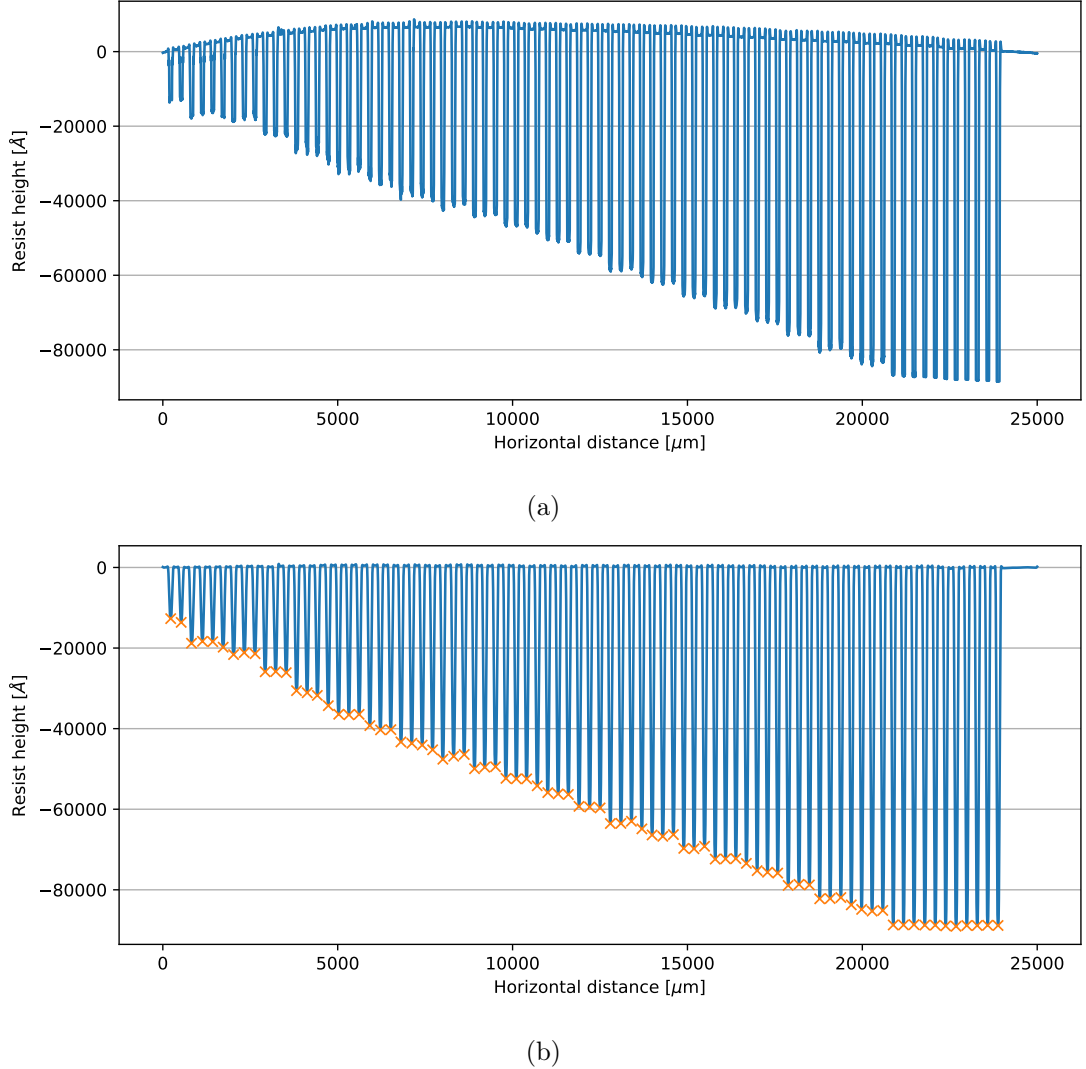


Figure 6.1: A comparison between (a) the raw height profile from the profilometer and (b) the filtered signal with curvature removed and valleys identified (orange crosses) by the SciPy signal module [46]. The height difference is used to generate the calibration curve in figure 5.5, assuming an initial resist thickness of 8.77  $\mu\text{m}$  [44].

Each shape can be defined by a height profile function:

$$h_{cir}(x, y, R, h_0) = h_0 - R + \sqrt{R^2 - x^2 - y^2} \quad (6.1)$$

$$h_{gau}(x, y, \sigma, h_0) = h_0 \cdot \exp\left(-\frac{x^2 + y^2}{2\sigma^2}\right) \quad (6.2)$$

$$h_{cos}(x, y, p, h_0) = \frac{h_0}{2} \cdot \left[1 + \cos\left(\frac{2\pi}{p} \cdot \sqrt{x^2 + y^2}\right)\right] \quad (6.3)$$

with  $\sigma$  being the standard deviation of the Gaussian function and  $p$  being the period of the cosine. Whereas the radius the curvature for a circular dome is trivial, we can find corresponding values for the Gaussian and Cosine shapes by equating second-order

Taylor expansions at the apex. We find the following relationships:

$$p = \sqrt{2\pi^2 Rh_0} \quad (6.4)$$

$$\sigma = \sqrt{Rh_0} \quad (6.5)$$

and hence all domes can be uniquely characterized by radius  $R$  and apex height  $h_0$ , up to horizontal translation. We can estimate the parameters by performing least squares regression of the desired shape function on the profilometer output, as shown in figure 6.2. We can start quantifying the quality of the domes by using figures of merit. An easy way is to check the relative difference in the dome's defining parameters:

$$\Delta h = \frac{h_{fit} - h_{exp}}{h_{exp}} \quad (6.6)$$

$$\Delta R = \frac{R_{fit} - R_{exp}}{R_{exp}} \quad (6.7)$$

where the  $exp$  subscript indicates the expected parameters (radius and apex height) and the  $fit$  subscript indicates the values obtained from the least squares regression.

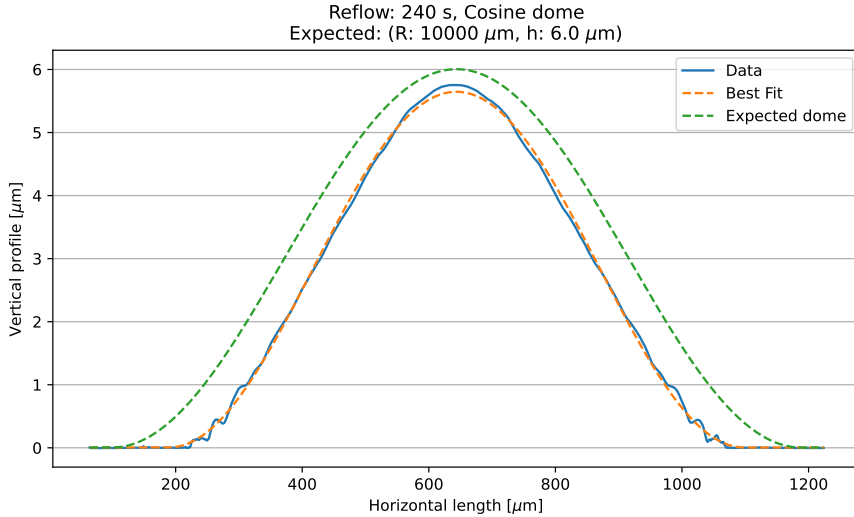


Figure 6.2: Estimating the height and radius of a sample dome (in this case, a cosine dome with  $R = 10000 \mu\text{m}$ ,  $h = 6.0 \mu\text{m}$  after 240 seconds of solvent reflow). using least squares regression (fitted function is the orange dashed line) on the profilometer output (blue solid line). Vertical and horizontal offset are also parameters in the regression, and the expected dome height function (green dashed line) uses their optimal values. The current dome has a apex height  $h_{fit} = 5.6 \mu\text{m}$  and an effective radius of curvature  $R_{fit} = 7438 \mu\text{m}$ .

Over several calibration runs optimizing the solvent reflow we were able to measure 400 different domes, with between 50 and 60 independent dome measurements for each reflow time; a scatter plot summarizing the statistical distribution is presented in figure 6.3, with accompanying marginal distributions and black dashed lines indicating the ideal values. Whereas on average we have a relative deviation on the order of 10%, the marginal distributions exhibit large tails.

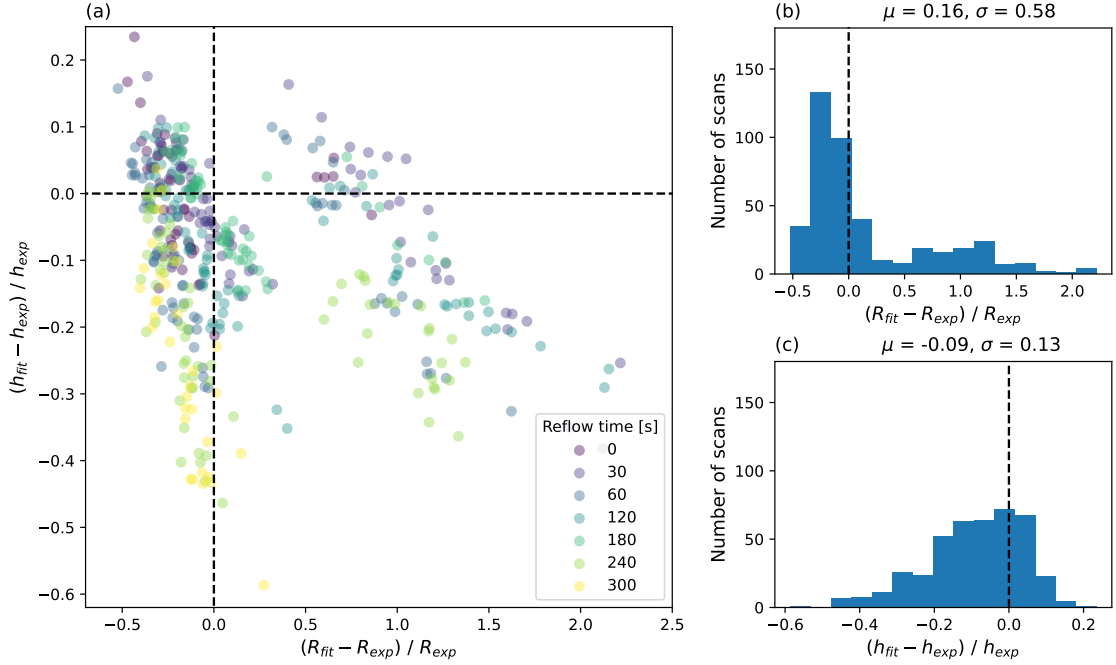


Figure 6.3: (a) Scatter plots showing the relative distribution of domes identified by reflow time, with the marginal distributions of (b) radii and (c) apex heights presented with their mean and standard deviations. The black lines correspond to the case where the height and radius of curvature from the fitted function match its expected counterparts.

### 6.1.3 Calibration correction

Even though we performed a new height calibration (as shown in figure 5.5), the results were not available for the design of the test structures, as these and the calibration array were both written on the same mask. We decided to use the calibration function from previous work [42], which assumed a linear relation between height and effective dose:

$$h_{prev}(d) = -0.0396 \cdot d + 8.46 \quad (6.8)$$

$$d_{prev}(h) = \frac{8.46 - h}{0.0396} \quad (6.9)$$

A second iteration of the mask based on the new calibration would surely yield better results; however, we can estimate a height correction for the profiles. Looking at figure 5.6, the height correction is simply the difference between the old and new calibration profiles (red and black dashed lines, respectively). On a more functional approach, we can estimate the corrected height as:

$$h_{corr}(p(x)) = h_{prev}(d_{EVG}(p(x))) \quad (6.10)$$

which is just the composition of the functions defined in equations 5.8 and 6.8 and  $p(x)$  is the profilometer measurement at point  $x$ . In essence, we are translating the profilometer height profile to the one that would be generated if we had designed our test structures using equation 5.8. Given that the functions have different zero crossings, we will ignore any points below  $1 \mu\text{m}$ ; otherwise, we will displace the regions without resist upwards, effectively changing the vertical offset calibration.

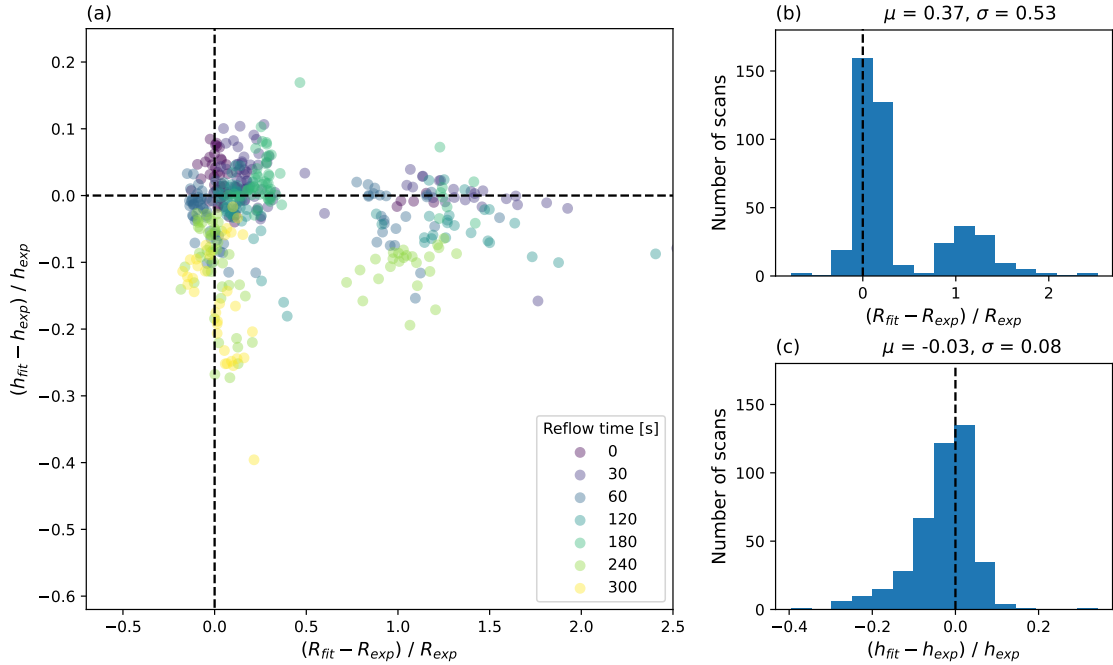


Figure 6.4: **Dome properties after calibration correction,** (a) Scatter plots showing the relative distribution of domes identified by reflow time, with the marginal distributions of (b) radii and (c) apex heights presented with their mean and standard deviations. The black lines correspond to the case where the height and radius of curvature from the fitted function match its expected counterparts.

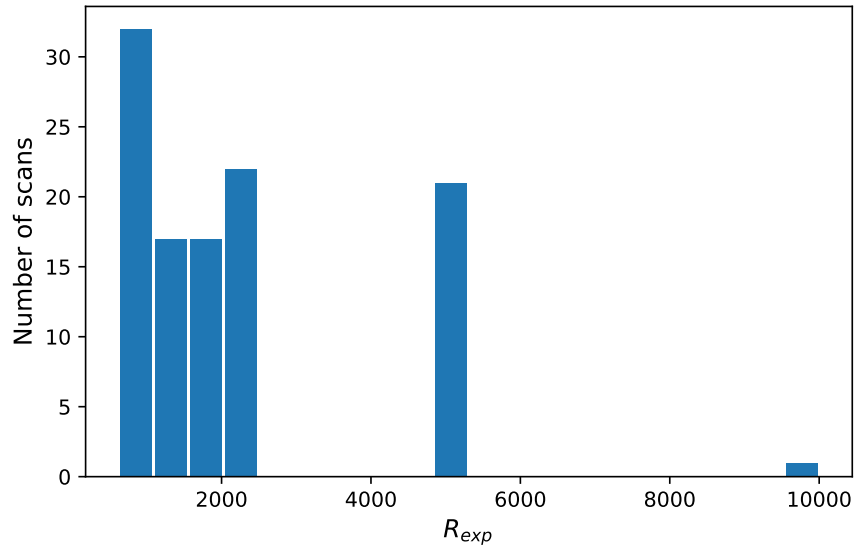


Figure 6.5: Radial distribution of outliers ( $R_{fit} > 1.5 \cdot R_{exp}$ ) in the corrected scatterplot shown in figure 6.4.

If we apply the calibration corrections to the profiles, the scatter plots in figure 6.3 change significantly, as seen in figure 6.4. The distribution is much more concentrated to the ideal case, and the standard deviations on both marginal distributions are reduced. Nevertheless, it is still possible to identify an outlier cluster on the right. We shall take a closer look to see whether we can find an explanation. Further analysis identified the outliers ( $R_{fit} > 1.5 \cdot R_{exp}$ ) in the corrected scatterplots to be predominantly circular domes of low radius of curvature, as seen in figure 6.5. No correlation was found regarding height.

The relative distributions of height and radius give a general overview of the fabrication quality; yet, they do not take into account the rest of the dome profile. Following previous work [42, 47], we define the normalized cross correlation coefficient  $r_{NCC}$  and the root mean square roughness  $r_{RMS}$ :

$$r_{NCC} = \frac{\sum_{m=1}^N p(x_m) h_e(x_m)}{\sqrt{\left(\sum_{k=1}^N p(x_k)^2\right) \cdot \left(\sum_{l=1}^N h_e(x_l)^2\right)}} \quad (6.11)$$

$$r_{RMS} = \sqrt{\frac{1}{N} \sum_{m=1}^N [p(x_m) - h_f(x_m)]^2} \quad (6.12)$$

where  $p(x_i)$  is the profilometer output at measurement point  $x_i$ ,  $h_e(x_i)$  and  $h_f(x_i)$  are the expected and best fit height profiles. Cauchy Schwarz inequality implies that  $r_{NCC} \in [-1, 1]$ , with +1 indicating complete cross correlation (i.e. profile and expected function match) and 0 indicating no correlation (i.e. profile and expected function **do not** match). The surface roughness measures the average deviation from the height profile; we wish to minimize this quantity as much as possible.

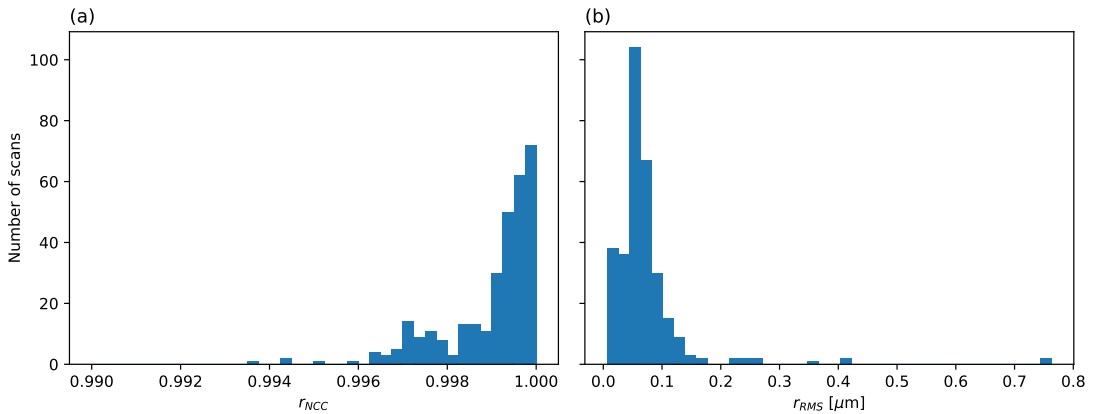


Figure 6.6: Histograms detailing the distributions of the (a) normalized cross correlation coefficient  $r_{NCC}$  and (b) the root mean square roughness  $r_{RMS}$  for domes produced in the mask aligner over different reflow times.

Now discarding the outliers ( $R_{fit} > 1.5 \cdot R_{exp}$ ), we can also see the expected marginal distributions for these figures of merit, shown in figure 6.6. The normalized cross correlation coefficient  $r_{NCC}$  exhibits a distribution centered around 0.999 with standard deviation of 0.002. The root mean square roughness  $r_{RMS}$  exhibits a distribution centered around 0.072  $\mu\text{m}$  with standard deviation of 0.074  $\mu\text{m}$ . Here we are considering

all domes over all reflow times; the dependence of the figures of merit on the latter is further examined in the next subsection.

#### 6.1.4 Reflow optimization

We wish to see how these two figures of merit evolve under reflow. We have chosen to perform reflow in steps of 60 seconds, with an additional step at 30s. We have calculated the mean and standard deviations of both  $r_{NCC}$  and  $r_{RMS}$  for each reflow step, and the results can be summarized in figure 6.7. As we can see,  $r_{NCC}$  does not change significantly, but the variance decreases significantly under just 30 seconds of solvent reflow. The root mean square roughness, on the other hand, decreases significantly, apparently stabilizing at 240 seconds; the variance decreases monotonically. Based on these results, we recommend a reflow time between 240 and 300 seconds to optimize figures of merit.

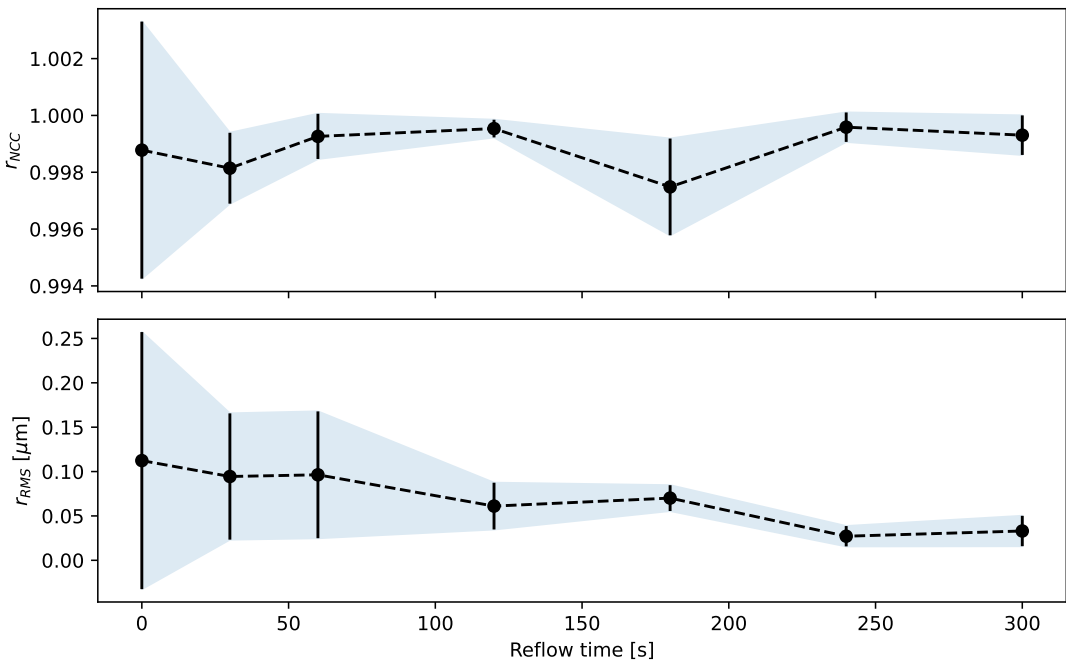


Figure 6.7: Evolution of figures of merit under reflow time. The dashed line corresponds to the mean and the shaded areas correspond to values within one standard deviation of the mean.

## 6.2 Direct written laser lithography

Using the direct laser written lithography technique, we produced a set of domes on the laser writer and subjected them to 300 seconds of solvent reflow. Due to the reduced output, we were only able to produce Gaussian and Cosine dome shapes with varying radius of curvature. We can further investigate the surface roughness by performing an atomic force microscopy scan on the top of a dome, as shown in figure 6.9. The calculated root mean square roughness for each case is 0.15 and 0.20 nm, respectively. These values lie close to the AFM's resolution limit, indicating the possibility that the values could be even smaller.

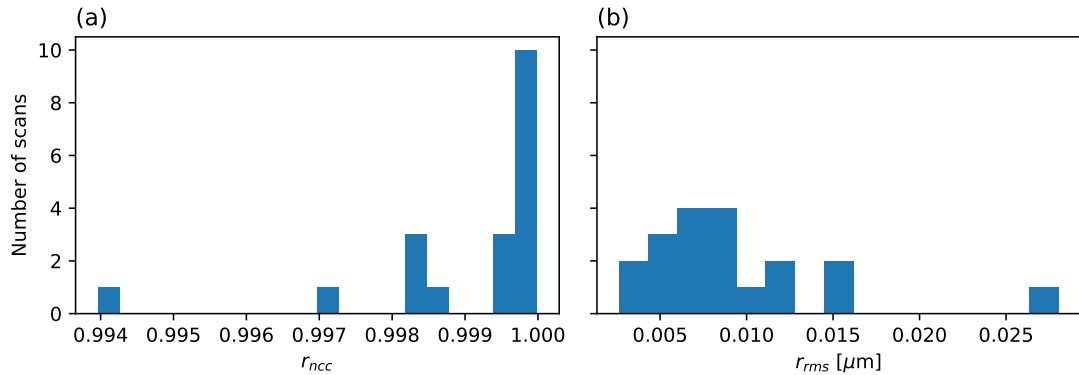


Figure 6.8: Histograms detailing the distributions of the (a) normalized cross correlation coefficient  $r_{NCC}$  and (b) the root mean square roughness  $r_{RMS}$  for domes produced in the laser writer.

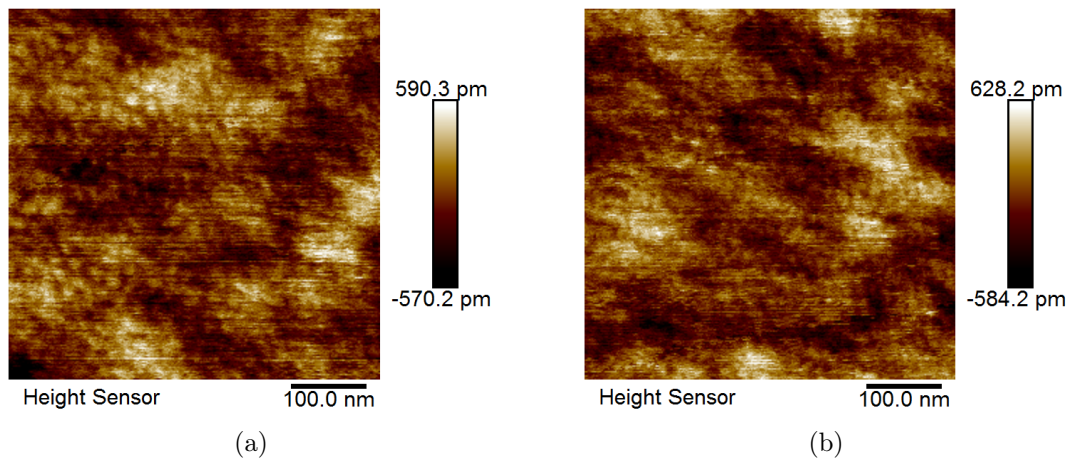


Figure 6.9: Atomic force microscopy (AFM) scans on the top of the direct laser written domes under 300 seconds of reflow. The calculated root mean square roughness for each case is 0.15 and 0.20 nm, respectively. These values lie close to the AFM's resolution limit, indicating the possibility that the values could be even smaller.

# Chapter 7

## Conclusion

Summarizing our results, we present two different methods to effectively simulate HBARs of different geometries and different materials, one based on the numerical solution to the corresponding eigenproblem, and the other based on the principle of the eigenstates being resonant solutions of an input field with non-zero spatial overlap to the mode. We see the spectral changes match the theoretical predictions in both cases. Furthermore, we also see that anharmonicities can change the structure of the spectrum; positive changes spreads out the energy levels, whereas negative changes concentrates them closer to ground state. For the envisioned goal of mode selectivity, both approaches can be useful:

- Positive anharmonicities displace the higher-level modes above further away from the ground state, which reduces the off-resonant couplings to those unwanted modes. One must be however careful, as the modes from previous FSRs can be pushed to higher energies exceeding the FSR; in figure 4.6 this would correspond to the cyan energy levels going to the right beyond the orange lines.
- Negative anharmonicities bunches them closer to the ground state. However, the envisioned goal of freeing up some space in the spectrum could not be achieved, as the processes also affects previously unbound modes which become bound due to the lowering of the energy level.

From the nanofabrication point of view, we see that grayscale lithography provides us more freedom on the choice of dome shapes. Masked grayscale lithography yields acceptable results that can be further corrected with an optimized time of solvent reflow (which reduces the root mean square roughness to the 100 nm level), and is therefore a suitable candidate for the mass production of domes. We see improved accuracy for domes with bigger radii ( $> 2000 \mu\text{m}$ ). On the other hand, despite being slower, direct-written laser lithography does provide better results, which can be used to generate high quality samples with root mean square roughness at the sub-nm level.

## 7.1 Outlook

In this work we have mainly focused on the HBARs, but we still have not assessed the couplings to other quantum-mechanical systems, which is one of the main motivations for the project. The frameworks defined here can be used to optimize the opto-mechanical interactions to specific cases by leveraging the spatial selectivity. This point was briefly illustrated in section 4.3.2, where we tuned our input field to match the spatial profile of the lowest Eigenmode (see figure 4.15). For our specific case [26], this translates in designing different shapes for the microwave antennas and piezoelectric layers; one could even assess convex-convex architectures with a piezoelectric disk on one side and an optimized dome shape on the other.

# Bibliography

- [1] N. Loubet, T. Hook, *et al.*, “Stacked nanosheet gate-all-around transistor to enable scaling beyond finfet,” in *2017 Symposium on VLSI Technology*, pp. T230–T231, 2017.
- [2] T. Ihn, *Semiconductor nanostructures : quantum states and electronic transport*. Oxford: Oxford University Press, 2010.
- [3] P. W. Shor, “Polynomial-time algorithms for prime factorization and discrete logarithms on a quantum computer,” *SIAM Journal on Computing*, vol. 26, pp. 1484–1509, oct 1997.
- [4] L. K. Grover, “A fast quantum mechanical algorithm for database search,” in *Proceedings of the Twenty-Eighth Annual ACM Symposium on Theory of Computing*, STOC ’96, (New York, NY, USA), p. 212–219, Association for Computing Machinery, 1996.
- [5] E. Farhi, J. Goldstone, S. Gutmann, and M. Sipser, “Quantum computation by adiabatic evolution,” 2000.
- [6] Y. Cao, J. Romero, *et al.*, “Quantum chemistry in the age of quantum computing,” *Chemical Reviews*, vol. 119, no. 19, pp. 10856–10915, 2019. PMID: 31469277.
- [7] X. Mi, M. Ippoliti, *et al.*, “Time-crystalline eigenstate order on a quantum processor,” *Nature*, vol. 601, pp. 531–536, nov 2021.
- [8] M. H. Devoret, B. Huard, R. Schoelkopf, and L. F. Cugliandolo, eds., *Quantum machines: Measurement and control of engineered quantum systems*. Lecture Notes of the Les Houches Summer School, London, England: Oxford University Press, June 2014.
- [9] A. Blais, A. L. Grimsmo, S. M. Girvin, and A. Wallraff, “Circuit quantum electrodynamics,” *Reviews of Modern Physics*, vol. 93, may 2021.
- [10] F. Arute, K. Arya, *et al.*, “Quantum supremacy using a programmable superconducting processor,” *Nature*, vol. 574, pp. 505–510, Oct 2019.
- [11] Y. Wu *et al.*, “Strong quantum computational advantage using a superconducting quantum processor,” *Phys. Rev. Lett.*, vol. 127, p. 180501, Oct 2021.
- [12] S. Pezzagna and J. Meijer, “Quantum computer based on color centers in diamond,” *Applied Physics Reviews*, vol. 8, no. 1, p. 011308, 2021.

- [13] J. P. Home, D. Hanneke, J. D. Jost, J. M. Amini, D. Leibfried, and D. J. Wineland, “Complete methods set for scalable ion trap quantum information processing,” *Science*, vol. 325, no. 5945, pp. 1227–1230, 2009.
- [14] S. Slussarenko and G. J. Pryde, “Photonic quantum information processing: A concise review,” *Applied Physics Reviews*, vol. 6, p. 041303, dec 2019.
- [15] L. S. Madsen, F. Laudenbach, M. F. Askarani, *et al.*, “Quantum computational advantage with a programmable photonic processor,” *Nature*, vol. 606, pp. 75–81, June 2022.
- [16] H.-S. Zhong, H. Wang, *et al.*, “Quantum computational advantage using photons,” *Science*, vol. 370, no. 6523, pp. 1460–1463, 2020.
- [17] G. S. MacCabe, H. Ren, *et al.*, “Nano-acoustic resonator with ultralong phonon lifetime,” *Science*, vol. 370, no. 6518, pp. 840–843, 2020.
- [18] M. J. Bereyhi, A. Arabmoheghi, A. Beccari, *et al.*, “Perimeter modes of nanomechanical resonators exhibit quality factors exceeding  $10^9$  at room temperature,” *Phys. Rev. X*, vol. 12, p. 021036, May 2022.
- [19] Y. Chu and S. Gröblacher, “A perspective on hybrid quantum opto- and electromechanical systems,” *Applied Physics Letters*, vol. 117, p. 150503, Oct. 2020.
- [20] Y. Chu, P. Kharel, T. Yoon, L. Frunzio, P. T. Rakich, and R. J. Schoelkopf, “Creation and control of multi-phonon fock states in a bulk acoustic-wave resonator,” *Nature*, vol. 563, pp. 666–670, Nov. 2018.
- [21] B. M. Brubaker, J. M. Kindem, M. D. Urmey, *et al.*, “Optomechanical ground-state cooling in a continuous and efficient electro-optic transducer,” 2021.
- [22] M. Mirhosseini, A. Sipahigil, M. Kalaei, and O. Painter, “Superconducting qubit to optical photon transduction,” *Nature*, vol. 588, pp. 599–603, Dec. 2020.
- [23] A. N. Cleland, *Foundations of nanomechanics*. Advanced Texts in Physics, Berlin, Germany: Springer, May 2011.
- [24] W. Martienssen and H. Warlimont, eds., *Springer Handbook of Condensed Matter and Materials Data*. Springer Berlin Heidelberg, 2005.
- [25] W. H. Renninger, P. Kharel, R. O. Behunin, and P. T. Rakich, “Bulk crystalline optomechanics,” *Nature Physics*, vol. 14, pp. 601–607, Apr. 2018.
- [26] U. von Lüpke, Y. Yang, M. Bild, L. Michaud, M. Fadel, and Y. Chu, “Parity measurement in the strong dispersive regime of circuit quantum acoustodynamics,” *Nature Physics*, May 2022.
- [27] P. Kharel, Y. Chu, M. Power, W. H. Renninger, R. J. Schoelkopf, and P. T. Rakich, “Ultra-high-q phononic resonators on-chip at cryogenic temperatures,” *APL Photonics*, vol. 3, p. 066101, June 2018.
- [28] B. P. Newberry and R. B. Thompson, “A paraxial theory for the propagation of ultrasonic beams in anisotropic solids,” *The Journal of the Acoustical Society of America*, vol. 85, pp. 2290–2300, June 1989.

- [29] C. De Boor, *A practical guide to splines*. Applied Mathematical Sciences, New York, NY: Springer, 1 ed., Nov. 2001.
- [30] B. E. A. Saleh and M. C. Teich, *Fundamentals of photonics*. Wiley series in pure and applied optics, Singapore: Wiley, 2nd ed. ed., 2007.
- [31] A. G. Fox and T. Li, “Resonant modes in a maser interferometer,” *The Bell System Technical Journal*, vol. 40, no. 2, pp. 453–488, 1961.
- [32] J. W. Jaeken and S. Cottenier, “Solving the christoffel equation: Phase and group velocities,” *Computer Physics Communications*, vol. 207, pp. 445–451, 2016.
- [33] C. R. Harris, K. J. Millman, S. J. van der Walt, *et al.*, “Array programming with NumPy,” *Nature*, vol. 585, pp. 357–362, Sept. 2020.
- [34] H. Gomersall, “PyFFTW: A pythonic python wrapper around FFTW.” <https://github.com/pyFFTW/pyFFTW>, 2021.
- [35] M. Frigo and S. G. Johnson, “The design and implementation of fftw3,” *Proceedings of the IEEE*, vol. 93, no. 2, pp. 216–231, 2005.
- [36] “concurrent.futures — Launching parallel tasks — Python 3.10.7 documentation.” <https://docs.python.org/3/library/concurrent.futures.html>, 2022.
- [37] M. A. M. Marte and S. Stenholm, “Paraxial light and atom optics: The optical schrödinger equation and beyond,” *Phys. Rev. A*, vol. 56, pp. 2940–2953, Oct 1997.
- [38] P. W. Milonni, A. D. Bandrauk, and S. C. Wallace, *Optical Analogs of Model Atoms in Fields*, pp. 45–51. Boston, MA: Springer US, 1992.
- [39] R. B. Lehoucq, D. C. Sorensen, and C. Yang, *ARPACK users' guide - solution of large-scale eigenvalue problems with implicitly restarted Arnoldi methods*. Software, environments, tools, SIAM, 1998.
- [40] Y. Qiu, “Spectra: C++ Library For Large Scale Eigenvalue Problems.” <https://github.com/yixuan/spectra>, 2022.
- [41] F. Schwabl, *Quantum Mechanics*. Berlin, Germany: Springer, 4 ed., Sept. 2007.
- [42] T. W. J. Palmen, “Grayscale Lithography For The Fabrication Of  $\hbar$ BARs,” Master’s thesis, ETH Zürich, October 2021.
- [43] M. J. Madou, *Fundamentals of Microfabrication*. Boca Raton, FL: CRC Press, sep 1997.
- [44] Microchemicals GmbH, “Technical datasheet - AZ 4500 Series,” 2021.
- [45] J. Loomis, D. Ratnayake, C. McKenna, and K. M. Walsh, “Grayscale lithography—automated mask generation for complex three-dimensional topography,” *Journal of Micro/Nanolithography, MEMS, and MOEMS*, vol. 15, p. 013511, Mar. 2016.
- [46] P. Virtanen, R. Gommers, *et al.*, “SciPy 1.0: Fundamental Algorithms for Scientific Computing in Python,” *Nature Methods*, vol. 17, pp. 261–272, 2020.
- [47] D. J. Whitehouse, *Surfaces and their Measurement*. Kogan Page Science paper edition, Oxford, England: Hermes Penton, July 2004.

## Declaration of originality

The signed declaration of originality is a component of every semester paper, Bachelor's thesis, Master's thesis and any other degree paper undertaken during the course of studies, including the respective electronic versions.

Lecturers may also require a declaration of originality for other written papers compiled for their courses.

---

I hereby confirm that I am the sole author of the written work here enclosed and that I have compiled it in my own words. Parts excepted are corrections of form and content by the supervisor.

**Title of work** (in block letters):

Engineering Eigenstates in High-Overtone Bulk Acoustic Resonators

**Authored by** (in block letters):

*For papers written by groups the names of all authors are required.*

Name(s):

Rosso Gómez

First name(s):

Pedro

With my signature I confirm that

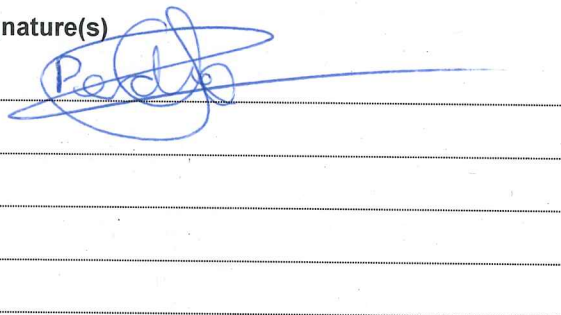
- I have committed none of the forms of plagiarism described in the 'Citation etiquette' information sheet.
- I have documented all methods, data and processes truthfully.
- I have not manipulated any data.
- I have mentioned all persons who were significant facilitators of the work.

I am aware that the work may be screened electronically for plagiarism.

Place, date

Zurich, 26.08.2022

Signature(s)



*For papers written by groups the names of all authors are required. Their signatures collectively guarantee the entire content of the written paper.*